

## Characterisation of SuperNEMO demonstrator calorimeter timing performance Study of $^{208}\text{TI}$ background rejection influence on the $0\nu\beta\beta$ decay sensitivity

Thèse de doctorat de l'Université Paris-Saclay  
préparée à l'Université Paris Saclay au sein du Laboratoire Irène-Joliot Curie  
(anciennement Laboratoire de l'Accélérateur Linéaire)

École doctorale n°576 Particles, Hadrons, Energy, Nuclei,  
Instrumentation, Imaging, Cosmos et Simulation (PHENIICS)  
Spécialité de doctorat : Physique des particules

Thèse présentée et soutenue à Orsay, le 11 décembre 2020, par

**CLOÉ GIRARD-CARILLO**

### Composition du Jury :

Alessandra Tonazzo APC - Paris	Rapporteuse
Mark C. Chen Queen's University	Rapporteur
Christine Marquet CENBG - Bordeaux-Gradignan	Examinatrice
Achille Stocchi LAL - Orsay	Examineur
Laurent Simard LAL - Orsay	Directeur de thèse
Mathieu Bongrand LAL - Orsay	Co-directeur de thèse





---

# Contents

Acknowledgement	3
Contents	5
Introduction	9
<b>1 Phenomenology of particle physics</b>	<b>11</b>
1.1 The Standard Model of particle physics . . . . .	11
1.1.1 Bosons . . . . .	11
1.1.2 Fermions . . . . .	11
1.1.3 $2\nu\beta\beta$ decay . . . . .	11
1.1.4 Where the Standard Model ends . . . . .	11
1.2 Going beyond the Standard Model with neutrinos . . . . .	11
1.2.1 Neutrino flavors and oscillations . . . . .	11
1.2.2 Neutrino masses and nature . . . . .	11
1.2.3 Neutrinoless double beta decay . . . . .	11
1.2.4 Other searches beyond the Standard Model with neutrinos .	11
1.3 $0\nu\beta\beta$ experiment status . . . . .	11
1.3.1 Experimental design criteria . . . . .	11
1.3.2 $0\nu\beta\beta$ direct search experiments . . . . .	13
1.3.3 Bolometers . . . . .	14
1.3.4 Time projection chambers . . . . .	14
1.3.5 Scintillators . . . . .	15
1.3.6 Tracking calorimeters . . . . .	17
<b>2 The SuperNEMO demonstrator</b>	<b>19</b>
2.1 The SuperNEMO technology . . . . .	20
2.1.1 Detection principle . . . . .	20
2.1.2 The source foils . . . . .	22
2.1.3 The tracker . . . . .	25
2.1.4 The calorimeter . . . . .	29
2.1.5 The magnetic coil and the shieldings . . . . .	34
2.1.6 Calibration strategy . . . . .	35

2.1.7	Detector cabling . . . . .	37
2.1.8	Electronics . . . . .	39
2.1.9	Detector gas tightness . . . . .	42
2.2	Backgrounds . . . . .	44
2.2.1	Internal background . . . . .	44
2.2.2	External background . . . . .	46
2.2.3	Radon background . . . . .	47
2.2.4	Background reduction . . . . .	48
2.3	The SuperNEMO software . . . . .	48
2.3.1	Simulation . . . . .	49
2.3.2	Reconstruction pipeline . . . . .	49
2.3.3	Analysis tools . . . . .	50
2.4	Conclusion . . . . .	53
<b>3</b>	<b>Sensitivity of the SuperNEMO demonstrator to the <math>0\nu\beta\beta</math></b>	<b>55</b>
3.1	The $0\nu\beta\beta$ signal and background model . . . . .	55
3.1.1	The $0\nu\beta\beta$ signal . . . . .	56
3.1.2	Inside detector backgrounds . . . . .	56
3.1.3	External backgrounds . . . . .	57
3.1.4	Expected number of decays . . . . .	58
3.2	Event selection . . . . .	59
3.2.1	Electron definition . . . . .	59
3.2.2	Total energy spectrum . . . . .	59
3.3	Demonstrator sensitivity to the $0\nu\beta\beta$ decay of $^{82}\text{Se}$ . . . . .	61
3.3.1	Sensitivity to the $0\nu\beta\beta$ half-life . . . . .	61
3.3.2	Limit on the effective neutrino mass . . . . .	63
3.4	Impact of sources contamination levels on the sensitivity . . . . .	65
3.4.1	Contamination levels . . . . .	65
3.4.2	Optimisation of event selection . . . . .	68
3.5	Impact of the magnetic field on the sensitivity . . . . .	74
3.5.1	Simulations of the magnetic field inside the demonstrator and reconstructed track fit . . . . .	74
3.5.2	Impact of the magnetic field on signal and background selections . . . . .	75
3.5.3	Influence of the magnetic field on optical modules and reconstruction efficiency . . . . .	77
3.5.4	Simulations with a non-uniform magnetic field . . . . .	78
3.6	Searching for the Neodymium-150 $0\nu\beta\beta$ decay . . . . .	80
3.6.1	Searching for the $0\nu\beta\beta$ of other isotopes . . . . .	80
3.6.2	Sensitivity to the $0\nu\beta\beta$ of $^{150}\text{Nd}$ . . . . .	80
3.7	The final detector sensitivity . . . . .	82
3.8	Conclusion . . . . .	83
<b>4</b>	<b>Improvement of the internal Thallium-208 background rejection</b>	<b>87</b>
4.1	Motivations . . . . .	87
4.2	The internal $^{208}\text{Tl}$ background . . . . .	88
4.2.1	The internal conversion process . . . . .	89

4.2.2	$^{208}\text{Tl}$ disintegrations in the 2e channel . . . . .	90
4.3	Simulated demonstrator performances . . . . .	90
4.4	Rejection of $^{208}\text{Tl}$ with a time-of-flight criterion . . . . .	92
4.4.1	The internal probability . . . . .	92
4.4.2	The exponential probability for $^{208}\text{Tl}$ events . . . . .	94
4.5	Event selection . . . . .	97
4.5.1	Energy selection . . . . .	97
4.5.2	Time-of-flight cut-off . . . . .	97
4.5.3	Probability cut-off . . . . .	99
4.5.4	Influence of the calorimeter time resolution . . . . .	102
4.6	Impact of $^{208}\text{Tl}$ rejection on the experiment's sensitivity . . . . .	103
4.6.1	Sensitivity results . . . . .	105
4.6.2	Expected number of background . . . . .	107
4.7	Conclusion . . . . .	108
<b>5</b>	<b>Calorimeter commissioning</b>	<b>111</b>
5.1	Optical modules calibration . . . . .	111
5.1.1	Pulse shape studies . . . . .	111
5.1.2	Baseline studies . . . . .	112
5.1.3	Gain studies . . . . .	112
5.1.4	Energy calibration . . . . .	113
5.2	Light Injection System . . . . .	114
5.3	Calorimeter cabling network . . . . .	116
5.3.1	Motivations . . . . .	116
5.3.2	Experimental setup . . . . .	117
5.3.3	Pulse shape analysis . . . . .	118
5.3.4	Pulse timing . . . . .	120
5.3.5	Signal attenuation . . . . .	125
5.3.6	Conclusion . . . . .	126
5.4	Synchronisation of calorimeter FEBs . . . . .	127
5.5	Conclusion . . . . .	129
<b>6</b>	<b>Characterisation of the calorimeter time resolution</b>	<b>131</b>
6.1	Interaction of particles in the SuperNEMO scintillators . . . . .	132
6.1.1	Interaction of electrons . . . . .	132
6.1.2	Interaction of photons . . . . .	132
6.2	Measurement of the time resolution with a $^{60}\text{Co}$ source . . . . .	133
6.2.1	Time response of optical modules . . . . .	134
6.2.2	Description of Cobalt 60 nucleus . . . . .	136
6.2.3	Experimental design . . . . .	137
6.2.4	Signal events selection . . . . .	139
6.2.5	Energy calibration . . . . .	141
6.2.6	Background estimation . . . . .	144
6.2.7	Determination of the individual timing resolution of each optical module . . . . .	148
6.2.8	Improvement of the method . . . . .	152
6.2.9	Conclusion . . . . .	152

6.3 The Light Injection System . . . . .	152
6.3.1 Light injection system commissioning . . . . .	152
6.3.2 Time resolution of optical modules . . . . .	152
<b>Conclusion</b>	<b>153</b>
<b>Résumé</b>	<b>155</b>
<b>Bibliography</b>	<b>157</b>





## Sensitivity of the SuperNEMO demonstrator to the $0\nu\beta\beta$

a study aiming to evaluate the SuperNEMO sensitivity to the  $0\nu\beta\beta$  decay, and the corresponding effective neutrino mass is presented. The final detector, based on the NEMO-3 technology, is expected to exclude half-lives up to  $1 \times 10^{26}$  y (90% CL), with an exposure of 500 kg.y with Selenium sources<sup>1</sup> [16]. The SuperNEMO demonstrator was designed in order to assess the technical feasibility of such a large-scale detector and to show that background specifications can be achieved. Its installation started in early 2015, at the Laboratoire Souterrain de Modane. With a reduced exposure of 17.5 kg.y, this demonstrator is expected to reach a sensitivity on the  $0\nu\beta\beta$  process of  $5.3 \times 10^{24}$  y (90% CL) [9].

As it was the case with its predecessor, a copper coil was designed to deliver a magnetic field inside the wire chamber, to bend the charged particles trajectories, hence making it possible to discriminate between electrons and positrons. However, studies led by the collaboration determined that this field could be impacted by the photomultiplier magnetic shields, producing notable variations in intensity and a loss of energy resolution [9][10]. We aim to explore the impact, on both the demonstrator and final detector sensitivity, of the presence of this magnetic field. The findings of this study participate in better understanding the detector performances. In a context of investigating the demonstrator and final detector's capabilities, different internal source contamination levels are considered. The topology of interest is that of two electrons, and we use the total energy sum to discriminate the signal from the background events. Thanks to SuperNEMO tracking capabilities, extra topological informations are exploited to improve the final sensitivity. To go further, we also explore the possibility of studying the  $0\nu\beta\beta$  decay of other  $\beta\beta$  isotopes.

### 3.1 The $0\nu\beta\beta$ signal and background model

A full GEANT4 simulation of the demonstrator was performed to determine, the lower limit on the  $0\nu\beta\beta$  half-life that can be probed with SuperNEMO in case

<sup>1</sup>Supposing the  $0\nu\beta\beta$  decay of  $^{82}\text{Se}$  occurs through the exchange of a light Majorana neutrino.

of the non-observation of the signal. Due to the time it would take to simulate every background contribution, we choose a simplified model. Indeed, only the most harmful backgrounds to the  $0\nu\beta\beta$  decay search were simulated. In addition,  $0\nu\beta\beta$  signal decays inside the detector were simulated, to better understand all the aspects of this analysis.

#### 3.1.1 The $0\nu\beta\beta$ signal

The SuperNEMO detector was designed to search for the yet never-observed  $0\nu\beta\beta$  decay. In the following, we assume the underlying mechanism for this decay is the exchange of a light Majorana neutrino, the so-called mass mechanism (MM), as it is the most widespread. The hypothetical  $0\nu\beta\beta$  signal would be detected as an excess of events at the end point of the  $2\nu\beta\beta$  spectrum, with respect to the predicted background contamination levels. Some  $10^7$   $0\nu\beta\beta$  events were simulated inside the source foils, using the DECAY0 software [17].

#### 3.1.2 Inside detector backgrounds

Numerous types of backgrounds that could mimic and hinder the search for the  $0\nu\beta\beta$  signal were simulated.

##### 3.1.2.1 Internal backgrounds

The so-called *internal backgrounds* stand for decays occurring inside the source foils, presenting the same signature as the  $0\nu\beta\beta$  signal. These backgrounds are mainly the  $2\nu\beta\beta$  decay undergone by the source isotope, disintegrations of  $^{208}\text{Tl}$  and  $^{214}\text{Bi}$  contaminations inside the source foils, as well as  $^{214}\text{Bi}$  disintegrations due to Radon deposited on the surface of the source foils.

#### The $2\nu\beta\beta$ process

In the full energy range, the allowed  $2\nu\beta\beta$  decay of  $^{82}\text{Se}$  stands as the dominant internal background type. The corresponding two-electrons energy sum spectrum is a continuum, whose ending point should stand at  $Q_{\beta\beta} = 2.99$  MeV, but is subtly shifted by the detector's energy resolution due to energy losses inside the source foils and gaseous detector. A total of  $10^7$  events of this decay were simulated inside the source foils, in the full energy window. However, above a certain energy value, the number of  $2\nu\beta\beta$  events decreases strongly, which can lead to a lack of statistics in a energy region favourable for the search for  $0\nu\beta\beta$  signal. To offset this effect, additional  $10^7$  of this decay were simulated on a slightly reduced energy range, that is to say above 2 MeV. The second set of simulations is normalised with the first one. In this way, the lack of  $2\nu\beta\beta$  simulated events in the high-energy tail is avoided, without requiring too high computational resources.

#### Source foils contamination by natural isotopes

As described in Sec. 2.2.1, after sources purification, residual natural isotopes such as  $^{208}\text{Tl}$  or  $^{214}\text{Bi}$  can still be present inside the foils, constituting the principal

internal source of background, with the  $2\nu\beta\beta$  decay. A total of  $10^7$  decays for each of the two isotopes were simulated inside the source foils.

### 3.1.2.2 Tracker contamination by natural isotopes

Radon, a descendant of  $^{238}\text{U}$ , is present as a gas in the tracker. Its daughter isotopes, when deposited on the tracker wires, can produce events similar to internal ones. In fact, one of the progeny of  $^{222}\text{Rn}$ , the  $^{214}\text{Bi}$ , can decay on (or near) a foil, and appear with a two-electron topology, becoming hard to distinguish from a double beta decay candidate. As this isotope is distributed throughout the whole tracking detection volume, a large quantity of this decay were simulated, that is to say  $10^8$  decays on the tracker wires.

### 3.1.3 External backgrounds

This background category was described in detail in Sec. 2.2.2. As a reminder, it is populated by the external  $\gamma$ -ray flux produced by radioactive isotope decays (mostly  $^{40}\text{K}$ ,  $^{214}\text{Bi}$  and  $^{208}\text{Tl}$ ) in detector components or surrounding laboratory rocks, as well as neutron interactions in the external iron shield. As simulating external backgrounds would be very consuming in terms of computing resources due to their very low probability to produce two electrons ( $2e$ ) topologies, let us check that this source of background is negligible. The NEMO-3 experiment set a limit on the external background number of counts, of  $< 0.2$  events in the  $2e$  topology, for the energy range  $[2.8;3.2]$  MeV (two electrons energy sum), for an exposure of  $34.3 \text{ kg}\cdot\text{y}$ , with  $^{100}\text{Mo}$  sources [18]. Recent radiopurity measurements of the SuperNEMO PMTs allow to conclude that the PMT  $^{214}\text{Bi}$  activity is 35% lower than for those of NEMO-3 [12], which is encouraging. Unfortunately, these measurements also revealed that the PMT budget in  $^{208}\text{Tl}$  isotope is 150% higher than NEMO-3. This could lead us to think that the external background contribution for SuperNEMO could be higher than that of NEMO-3. However, on that level, the most notorious difference between the two detectors is the fact that the SuperNEMO scintillator blocks are thicker than those of NEMO-3. Therefore, a gamma emitted from a PMT glass is more likely to be detected before crossing the source foils, such that it would be rejected and would not contribute to the background in the  $2e$  channel. Even if the regions of interest are slightly different between these two experiments, it produces a negligible increase on the external background contribution<sup>2</sup>. After all, given the fact that SuperNEMO is expected to be better than NEMO-3 at rejecting external background events, we consider that all external backgrounds from outside the foil, apart from  $^{222}\text{Rn}$  in the tracking volume, are expected to be negligible, and were not simulated.

---

<sup>2</sup>A study conducted by the SuperNEMO collaboration showed that at most 0.73 additional external background events would have been expected for the NEMO-3 detector, if instead of taking the  $[2.8;3.2]$  MeV energy range, we would have considered the  $[2.7;3.15]$  MeV region of interest.

### 3.1.4 Expected number of decays

The number of natural isotope decay events expected in the  $2e$  topology depends on their activities inside the source foils (for  $^{208}\text{Tl}$  and  $^{214}\text{Bi}$ ), or on the tracker's wires (for  $^{222}\text{Rn}$  decaying in  $^{214}\text{Bi}$ ). Therefore, it is mandatory to constrain the maximal tolerable activities for the detector [19]. The collaboration then established recommendations for maximum levels of the internal backgrounds, expressed in number of disintegrations per second, for a unit mass of  $\beta\beta$  isotope, or for a unit volume of gas. These *specified activities* have been calculated in order to achieve the expected sensitivity of the final detector.

The amount of expected double  $\beta$  decays is driven by its half-life value: the higher the half-life, the lower its contribution in the total number of expected background. For this analysis, we consider the  $2\nu\beta\beta$  half-life of  $^{82}\text{Se}$  measured by NEMO-3,  $T_{1/2}^{2\nu} = 9.39 \pm 0.17$  (stat)  $\pm 0.58$  (syst)  $\times 10^{19}$  years [20]. For the  $0\nu\beta\beta$  process, we also take the best limit set by the NEMO-3 detector,  $T_{1/2}^{0\nu} > 2.5 \times 10^{23}$  y [20]. This value is given for illustration purposes only, as it is not used to estimate the sensitivity of the detector.

Tab. 3.1 gives the expected number of background events, for the demonstrator and final detector exposures, assuming target background activities are reached:  $\mathcal{A}^{\text{Tl}} = 10 \mu\text{Bq/kg}$ ,  $\mathcal{A}^{\text{Bi}} = 2 \mu\text{Bq/kg}$  and  $\mathcal{A}^{\text{Rn}} = 0.15 \text{ mBq/m}^3$ . The expected

Process	Half-life/Activity	Expected decays	
		Demonstrator	Final detector
$2\nu\beta\beta$	$T_{1/2}^{2\nu} = 9.39 \times 10^{19} \text{ y}$	$9.5 \times 10^5$	$2.7 \times 10^7$
$^{208}\text{Tl}$	$\mathcal{A}^{\text{Tl}} = 2 \mu\text{Bq/kg}$	$1.1 \times 10^3$	$3.1 \times 10^4$
$^{214}\text{Bi}$	$\mathcal{A}^{\text{Bi}} = 10 \mu\text{Bq/kg}$	$5.5 \times 10^3$	$1.6 \times 10^5$
$^{222}\text{Rn}$	$\mathcal{A}^{\text{Rn}} = 0.15 \text{ mBq/m}^3$	$1.8 \times 10^5$	$7.2 \times 10^6$

Table 3.1: Expected number of background events, for the demonstrator (17.5 kg.y) and for the final detector (500 kg.y). We assume target background activities are reached:  $\mathcal{A}^{\text{Tl}} = 10 \mu\text{Bq/kg}$ ,  $\mathcal{A}^{\text{Bi}} = 2 \mu\text{Bq/kg}$ ,  $\mathcal{A}^{\text{Rn}} = 0.15 \text{ mBq/m}^3$ . The measured half-life  $T_{1/2}^{2\nu} = 9.39 \times 10^{19} \text{ y}$  for  $^{82}\text{Se}$  is considered [20].

number of disintegrations do not take into account any technique to reject background, and are given for the full energy range of the two measured electrons. Indeed, they are expected to be extremely reduced, notably by the application of event selections aimed at maximising the sensitivity to the  $0\nu\beta\beta$  half-life. Moreover, for the current sensitivity analysis, we focus on a narrow energy window, called *region of interest*, whose usefulness is described in detail in Sec. 3.2. This is also one of the reasons why it was necessary to simulate a large number of events, so that the signal and backgrounds are correctly represented in the region of interest.

## 3.2 Event selection

For SuperNEMO, the  $0\nu\beta\beta$  signature is two-electrons events, emitted simultaneously from the same vertex on the source foils, with an energy sum compatible with  $Q_{\beta\beta} = 2.99$  MeV for  $^{82}\text{Se}$  sources. Therefore, we conducted this analysis selecting only events matching the  $2e$  topology.

### 3.2.1 Electron definition

A reconstructed particle is tagged as an electron if it has:

- a vertex on the source foil,
- a reconstructed track inside the wire chamber,
- an associated calorimeter hit,
- and a final criterion depending on the charged particle curvature.

About the last point, as announced, we aim at studying the influence of the magnetic field on the final sensitivity results. To this end, we are led to consider two separate cases, one where the magnetic field is switched on, aligned with the  $Z$  (vertical) axis of the detector, with a uniform value of 25 Gauss, and one where it is switched off. In the first case, particles such as electrons and positrons of a few MeV have a curved trajectory in the tracker. In the second case, the tracks of the particles may be similar to straight lines (not to mention the possible multiple scattering on the wires of the tracker). It is then necessary to adapt the selection of events to each case. When the magnetic field is on, we consider a fourth criterion: a particle is identified as an electron if its track has a negative curvature<sup>3</sup>. In the following, we present results where the magnetic field is turned on. The off-field study is addressed in Sec. 3.5.

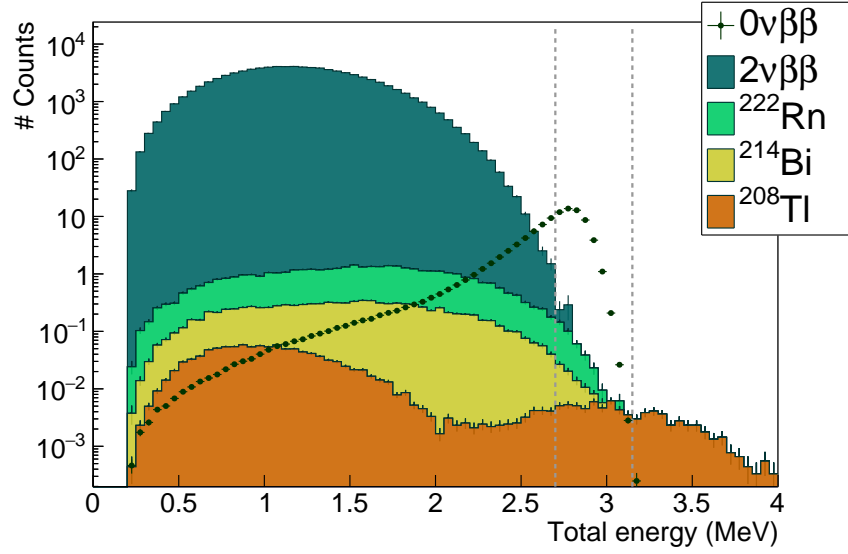
A two-electron ( $2e$ ) topology is then defined as two reconstructed tracks with negative curvatures, each one associated with a vertex on the source foils and a calorimeter hit. These selections represent the so-called *first-order* cut-offs. The  $2e$  topologies have been selected using the Particle Identification module at the end of the Falaise reconstruction pipeline [9]. I wrote my own module and added it to the collaboration software in order to store the selected events in a data format matching my off-line analysis chain. Second order selections taking into account topological information (time of flight, location of vertices on the source foils) are presented in Sec. 3.4.

### 3.2.2 Total energy spectrum

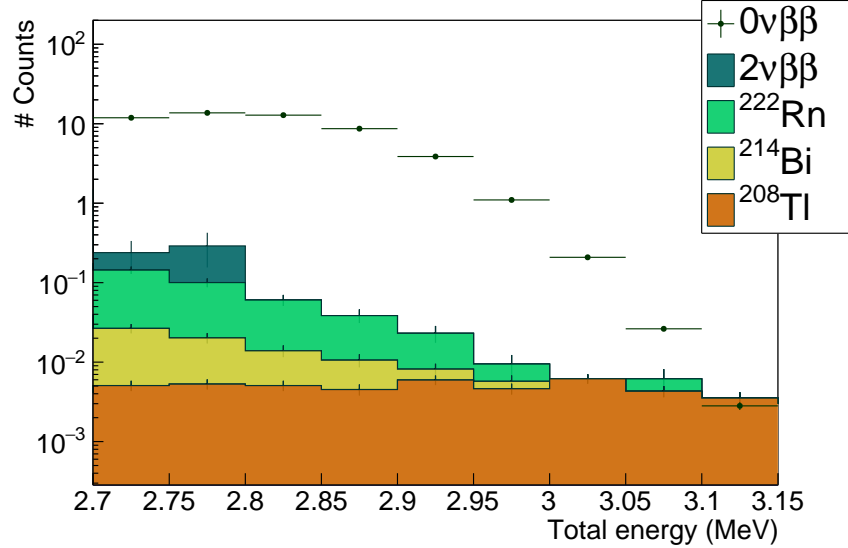
In Fig. 3.1, we present the total energy spectra for each simulated process in the  $2e$  topology, after application of the first-order cut-offs. The distributions are given

---

<sup>3</sup>A trajectory is said by convention to be negative if it has the same curvature as that of an electron moving from the source to the calorimeter, in a magnetic field oriented according to  $+Z$ .



(a) Full energy range.



(b) Zoom on ROI.

Figure 3.1: Total energy spectra for the  $0\nu\beta\beta$  signal and main backgrounds, for (a) the full energy range, and (b) for the  $[2.7;3.15]$  MeV energy range, whose optimisation is discussed in Sec. 3.3. The  $2\nu\beta\beta$  spectrum is normalised to  $T_{1/2}^{2\nu} = 9.39 \times 10^{19}$  y, and the specified activities are considered for  $^{208}\text{Tl}$ ,  $^{214}\text{Bi}$  and  $^{222}\text{Rn}$ . The amplitude of the  $0\nu\beta\beta$  is arbitrarily set at the limit obtained with NEMO-3.

for the demonstrator ( $^{82}\text{Se}$  sources, 17.5 kg.y exposure), considering the specified activities are reached. If the  $0\nu\beta\beta$  decay is detected, the two-electrons energy sum distribution would be a peak, located at the end-point of the  $2\nu\beta\beta$  energy distribution, that is to say at the total available energy,  $Q_{\beta\beta} = 2.99$  MeV. As the two electrons of this decay would share the total available energy, this peak should be infinitely thin. However, a widening of this distribution is expected, due to

energy losses inside the dense source material. Indeed, the path of an electron in the source is more or less long, depending on the disintegration location and on the emission angle, leading to a degradation of the measured energy. This peak is also expected to be shifted towards small energies, by the calorimeter energy resolution and the straggling of energy losses inside the wire chamber. Consequently, the  $0\nu\beta\beta$  energy distribution is expected to be asymmetrical, as displayed in the figure.

As explained in Sec. 3.1, two sets of  $2\nu\beta\beta$  events were simulated: one on the full energy range, and one for which the two-electrons energy sum is greater than 2 MeV. After the normalisation of these two sets, we get the complete  $2\nu\beta\beta$  energy spectrum displayed in the figure. The  $^{208}\text{Tl}$  total energy spectrum extends up to high energies. It reveals two distinct peaks, one corresponding to a low-energy  $\beta$  particle, the other to the internal conversion of the 2.614 MeV gamma, emitted after  $^{208}\text{Tl}$   $\beta^-$  disintegrations (Sec. 2.2.1). Whatever their origin, either  $^{222}\text{Rn}$  contaminations inside the tracker gas, or internal contaminations of the source foils, the two  $^{214}\text{Bi}$  energy distributions have nearly the same shapes.

These energy spectra confirm the  $2\nu\beta\beta$  background is dominant in the total energy range. Therefore, a widespread technique consists in constraining the  $0\nu\beta\beta$  decay searches to a narrow energy range, the so-called *region of interest* (ROI). It allows to reduce the total number background decays, while maximising the chances of observing the signal decay, then to maximise the limit set on  $T_{1/2}^{0\nu}$ . A typical ROI is materialised in the figure by two vertical dashed lines, revealing  $^{208}\text{Tl}$ ,  $^{214}\text{Bi}$  and  $^{222}\text{Rn}$  could be harmful for the search for the  $0\nu\beta\beta$  decay. The influence of the sources contamination by these natural isotopes, as well as optimised background rejection techniques are presented in Sec. 3.4.

In the following, we expose general principles leading to the determination of the best limit on  $T_{1/2}^{0\nu}$ , in the appropriate region of interest. We illustrate the reasoning by applying it on the demonstrator case, with specified activities, and on-magnetic field condition. However, the technique presented remain valid for all exposures, internal contamination levels and field conditions.

### 3.3 Demonstrator sensitivity to the $0\nu\beta\beta$ decay of $^{82}\text{Se}$

The SuperNEMO demonstrator is designed to measure  $\beta\beta$  decays of radioactive emitters. In case a the non-observation of the  $0\nu\beta\beta$  process, the collaboration would set an lower-limit on the half-life  $T_{1/2}^{0\nu}$ , and an upper-limit on the effective neutrino mass  $m_{\beta\beta}$ .

#### 3.3.1 Sensitivity to the $0\nu\beta\beta$ half-life

In case of the non-observation of a  $0\nu\beta\beta$  signal, the expected lower limit on the half-life is provided for a given energy range  $[E_{\min}; E_{\max}]$  on the two electrons energy sum, and depends on the characteristics of the detector. Firstly, it depends on the signal detection efficiency,  $\epsilon_{0\nu}$  in this energy window, which corresponds to



the ratio of the number of selected signal events to the number of simulated ones. It also depends on the source isotope nature, as well as on the detector exposure  $m \times t$ , with  $m$  the mass of source material in the foils and  $t$  the data acquisition time period. It follows

$$T_{1/2}^{0\nu} > \frac{\mathcal{N}_A \ln 2}{M} \times \frac{\epsilon_{0\nu} \times m \times t}{N_{0\nu}^{\text{excl.}}}, \quad (3.1)$$

with  $\mathcal{N}_A$  the Avogadro number and  $M$  the  $\beta\beta$  emitter molar mass.  $N_{0\nu}^{\text{excl.}}$  is the number of signal events excluded at a given confidence level (usually 90%), calculated with the Feldman-Cousins statistics from the total expected number of background events. The Feldman-Cousins statistics [21] is a wide-used method in rare events search experiments, providing confidence intervals for upper limits in the case of background events following a Poissonian probability law. We use this method in the framework of this analysis to provide a limit, at 90% CL, on the number of excluded signal events  $N_{0\nu}^{\text{excl.}}$ , on the basis of the expected number of background events, given below.

- The  $2\nu\beta\beta$  background

Eq. (3.1) defines the lower limit on  $T_{1/2}^{0\nu}$  from the number of excluded signal events, and the signal selection efficiency  $\epsilon_{0\nu}$ . In a similar manner, we can define the number of expected  $2\nu\beta\beta$  events,  $N_{2\nu}$ , from the half-life  $T_{1/2}^{2\nu}$  and the  $2\nu\beta\beta$  selection efficiency,  $\epsilon_{2\nu}$ , as

$$N_{2\nu} = \frac{\mathcal{N}_A \ln 2}{M} \times \frac{\epsilon_{2\nu} \times m \times t}{T_{1/2}^{2\nu}}. \quad (3.2)$$

- Natural radioactive backgrounds

We consider the background massic activities  $A_{\text{rad.}}$ , and  $\epsilon_{\text{rad.}}$  their selection efficiencies in a given energy window. The number of background events is therefore given, for the  $^{208}\text{Tl}$  and  $^{214}\text{Bi}$  internal contaminations, as

$$N_{\text{rad.}}^m = A_{\text{rad.}}^m \epsilon_{\text{rad.}}^m \times m \times t, \quad (3.3)$$

where  $A_{\text{rad.}}$  is given in Bq/kg. Similarly, for the  $^{222}\text{Rn}$  background,

$$N_{\text{rad.}}^V = A_{\text{rad.}}^V \epsilon_{\text{rad.}}^V \times V \times t, \quad (3.4)$$

with  $V = 15.3 \text{ m}^3$  the total tracker volume, and  $A_{\text{rad.}}$  represents here a volumic activity, given in Bq/ $\text{m}^3$ .

As we said, all equations from Eq. (3.1) to (3.4), are valid for a given energy range  $[E_{\text{min}}; E_{\text{max}}]$ . To find the optimal energy interval for the search for the  $0\nu\beta\beta$  decay, that is to say the one maximising the limit on  $T_{1/2}^{0\nu}$ , we must study the influence of the variations of  $E_{\text{min}}$  and  $E_{\text{max}}$  bounds on the final sensitivity. On Fig. 3.1, we observe that beyond the energy sum of 3 MeV, the total number of background events is highly reduced, and the  $^{208}\text{Tl}$  background dominates, with 0.03 count expected for  $E > 3.2 \text{ MeV}$ . This is why the upper limit  $E_{\text{max}}$  of the energy interval has only a limited impact on the search for the best ROI. It is then



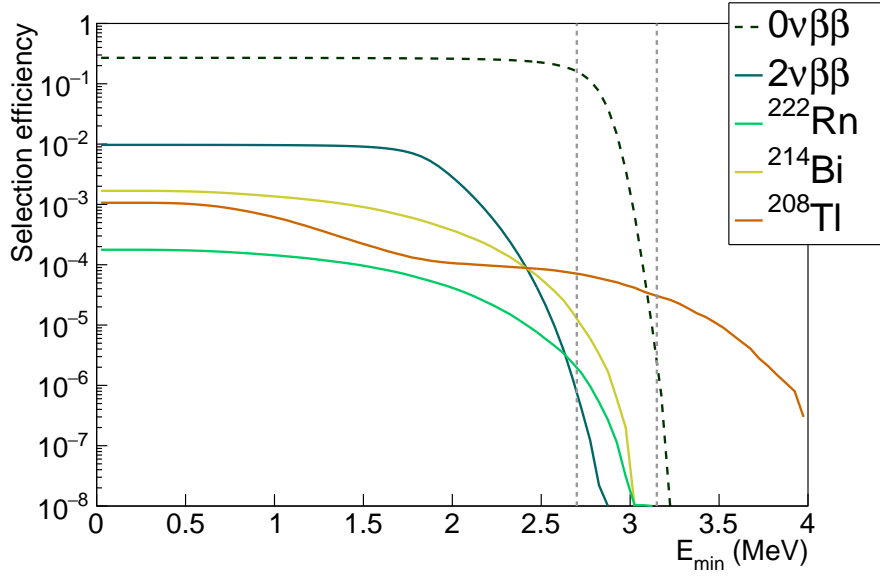


Figure 3.2: Efficiency spectra as a function of  $E > E_{\min}$ , for the  $0\nu\beta\beta$  signal (dashed black line) and for the main backgrounds (plain lines). The two vertical grey lines depict the final ROI optimised for the case of the demonstrator, taken the specified isotope activities.

natural to study mainly the influence of the lower limit  $E_{\min}$ . In that purpose, the selection efficiencies, entering in the calculation of the  $T_{1/2}^{0\nu}$  lower limit, are presented in Fig. 3.2, as a function of the lower bound  $E_{\min}$ . As a matter of fact, the ROI would correspond to an energy range where  $\epsilon_{0\nu}$  is high, and where selection efficiencies for the background are low, in order to maximise the  $T_{1/2}^{0\nu}$ . The variations of the limit set on  $T_{1/2}^{0\nu}$  (at 90 % CL) as a function of  $E_{\min}$  and  $E_{\max}$  are presented in Fig. 3.3. We found that, for the demonstrator exposure, with  $^{82}\text{Se}$  sources, with a 25 Gauss magnetic field, and for the specified background activities, the best ROI is [2.7;3.15] MeV. As expected, as long as the upper bound is larger than 3.15 MeV, the sensitivity on the search for  $0\nu\beta\beta$  is not affected. Therefore, this value is kept in order to enter into a future more general study, taking into account the neutron background of the experiment, which extends at high energies. Tab. 3.2 summarises the expected number of background events for each non-zero contamination case presented in Fig. 3.4.

In the optimised [2.7;3.15] MeV energy range, the sensitivity expected for the SuperNEMO demonstrator stands at

$$T_{1/2}^{0\nu} > 5.7 \times 10^{24} \text{ y} \quad (90\% \text{CL}). \quad (3.5)$$

This result is compatible with previous SuperNEMO analysis [9].

### 3.3.2 Limit on the effective neutrino mass

The decay rate for the light Majorana exchange mechanism is given by:

$$(T_{1/2}^{0\nu})^{-1} = g_A^4 G^{0\nu} |M^{0\nu}|^2 \left| \frac{m_{\beta\beta}}{m_e} \right|^2. \quad (3.6)$$

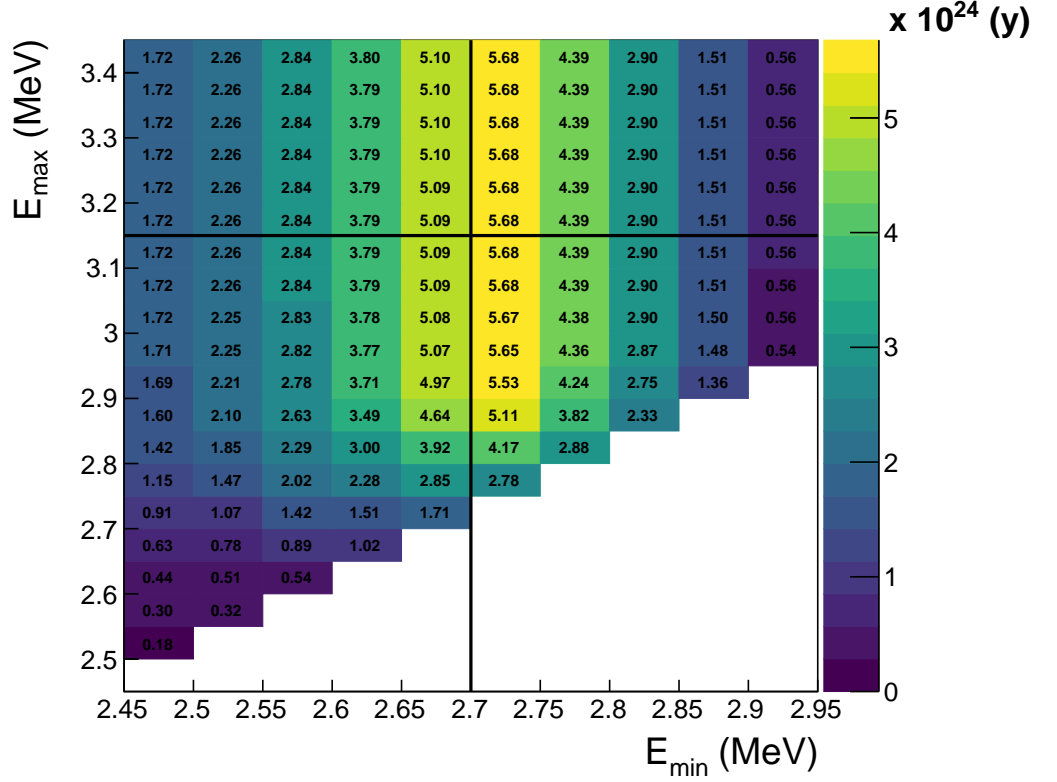


Figure 3.3: Two-dimensional histogram showing the evolution of the  $T_{1/2}^{0\nu}$  909% limit as a function of the lower and upper energy bounds. The maximal lower limit of  $T_{1/2}^{0\nu} > 5.7 \times 10^{24}$  y (90% CL) is retained, in the [2.7;3.15] MeV region of interest.

Process	Event selection
$\epsilon_{0\nu}$	14.7%
$2\nu\beta\beta$	0.418
$^{208}\text{Tl}$	0.0475
$^{214}\text{Bi}$	0.0546
$^{222}\text{Rn}$	0.292
Total	0.394

Table 3.2: Selection efficiency of  $0\nu\beta\beta$  events and expected number of backgrounds events in the optimised ROI [2.7;3.15] MeV, for the exposure of the SuperNEMO demonstrator (17.5 kg.y). The specified levels of contamination are considered.

where  $G^{0\nu}$  is the two particles phase space factors, depending on  $Q_{\beta\beta}$  and  $Z$  the number of protons,  $M^{0\nu}$  is the nuclear matrix elements for the  $0\nu\beta\beta$  process, and  $m_{\beta\beta}$  is the effective Majorana neutrino mass, defined as

$$\langle m_{\beta\beta} \rangle = |\sum_i m_i U_{ei}^2|, \quad (3.7)$$

where  $m_i$  are the neutrino masses, and  $U_{ei}^2$  is the mixing matrix. Therefore, the effective mass takes into account the neutrino mixing. Consequently, observing the

$0\nu\beta\beta$  decay would not only prove the Majorana nature of neutrinos but, assuming the mass mechanism, could also help constraining the absolute neutrino masses. Given  $g_A$ ,  $G^{0\nu}$  and  $M^{0\nu}$  [22, 23], we find the SuperNEMO demonstrator could reach a limit on the effective neutrino mass of

$$\langle m_{\beta\beta} \rangle < [0.24 - 0.47] \text{ eV} \quad (90\% \text{CL}). \quad (3.8)$$

Although this limit is not competitive with other current  $0\nu\beta\beta$  experiments, this is an improvement compared to NEMO-3, demonstrating that SuperNEMO's technology would benefit from being adapted to larger scales.

In this section, we presented the general procedure leading to an optimised result on the  $T_{1/2}^{0\nu}$  limit, and gave a result for the SuperNEMO demonstrator compatible with the previous studies led by the collaboration. Thereafter, we discuss the results obtained for different detector exposures (demonstrator and final detector), and different internal background activities. Also, and this is the main purpose of this study, we discuss the influence of the presence of the magnetic field on the final detector's sensitivity.

## 3.4 Impact of sources contamination levels on the sensitivity

We study the impact of the isotope contamination levels (inside the source foils, as well as on the tracker's wires) on the  $0\nu\beta\beta$  sensitivity. We also optimise additional event selections aimed at improving it.

### 3.4.1 Contamination levels

Strict specifications have been defined for source foil contamination in order to achieve the target sensitivity for the final SuperNEMO detector (500 kg.y). BiPo detector and SuperNEMO collaboration measurements (Sec. 2.2.1) have shown that the  $^{208}\text{Tl}$  level is not reached for the demonstrator source foils, being almost 27 times higher than expected, with  $\mathcal{A}^{\text{Tl}} = 54 \mu\text{Bq/kg}$  [26 - 102]. Also, the  $^{214}\text{Bi}$  contamination is not greater than  $290 \mu\text{Bq/kg}$  at 90% CL. If this upper limit was reached we would expect  $1.6 \times 10^5$  internal Bismuth events in the total energy range. Fortunately, the Radon contamination inside the wire chamber does not exceed the specifications supposing an gas flow rate of  $2 \text{ m}^3/\text{h}$  inside the chamber. In Sec. 3.3, we developed the general procedure allowing to set a 90% confidence interval limit on  $T_{1/2}^{0\nu}$ . For the demonstrator, supposing the specified activities are reached, the demonstrator would achieve a sensitivity of  $5.7 \times 10^{24}$  years on the searched decay, in 2.5 years of data acquisition, with 7 kg of  $^{82}\text{Se}$ . This sensitivity could be affected by the higher-than-specified levels of internal contaminations measured by BiPo.

In this sub-section, four distinct levels of internal contaminations are considered:

- the *zero activities* case, a hypothetical case where the source foils and the tracker are non contaminated at all by natural isotopes,

- the *specified activities* case, where the targeted level of contaminations would have been reached,
- and two *measured* cases. As the  $^{214}\text{Bi}$  activity is provided by BiPo measurements as an upper limit, we choose to present the results either for sources that would not be contaminated by this isotope (the *without  $^{214}\text{Bi}$*  case), or considering that the activity reached is  $290\text{ }\mu\text{Bq/kg}$  (*with  $^{214}\text{Bi}$* ). The  $^{208}\text{Tl}$  activity considered for these two measured cases is the limit at 90% CL.

The fact that we are showing results for a hypothetical zero isotope contamination is to illustrate an important phenomenon about the Feldman-Cousins statistics employed to determine the number of excluded signal events,  $N_{0\nu}^{\text{excl.}}$ , given the number of observed background events (defined from Eq. (3.2) to Eq. (3.4)).

**Clarifications on Feldman-Cousins statistics** When the expected number of background events is negligible (which is the case for the zero and specified levels), the probability  $p$  to observe  $n_s$  signal events, expecting  $s$  events, is given by the Poisson distribution

$$p = \frac{e^{-s} s^{n_s}}{n_s!} . \quad (3.9)$$

Let's now put ourselves in the situation where no signal event is observed - that is what we assume to put an lower limit on the  $0\nu\beta\beta$  half-life. Then  $n_s \rightarrow 0$ , and  $p \rightarrow e^{-s}$ . If zero signal event is *observed*, it is incorrect to assume that zero signal events were *produced* during the experiment. We only can say that no signal event has been observed *a priori*. To account for this particular case, the quantity  $s$  should no longer be viewed as the number of expected signal events, but as the number of excluded signal events,  $N_{0\nu}^{\text{excl.}}$ . In the end, for a negligible expected number of background events, and no signal event observed, we can set an lower limit on the number of excluded signal events, excluding values for which  $p < \alpha$ . Taking a 90% confidence interval, that is to say  $\alpha = 10\%$ , we obtain  $s \leq 2.303$ .

We show in Fig. 3.4 the 90 % CL  $T_{1/2}^{0\nu}$  limit for the four contamination levels considered, as well as the corresponding regions of interest, optimised following the technique explained in Sec. 3.3.. As expected from the previous conclusions given on the Feldman-Cousins statistics, no difference is observed in terms of half-life limits, or ROI, between the zero and specified activity cases. Now considering the two measured activity cases, the sensitivity is decreased compared with the specified case. Indeed, the number of background events in the ROI is no more negligible, and influence significantly the value of  $T_{1/2}^{0\nu}$ , decreasing the experiment's sensitivity by 23% (without  $^{214}\text{Bi}$ ) and 37% (with  $^{214}\text{Bi}$ ).

Tab. 3.3 summarises the expected number of background events for each non-zero contamination case presented in Fig. 3.4. Regions of interest, optimised for each activity, are reminded. The total number of background events for the specified activity case is negligible in this region. This is the reason why the limit of 2.303 on the number of excluded signal events is reached, according to

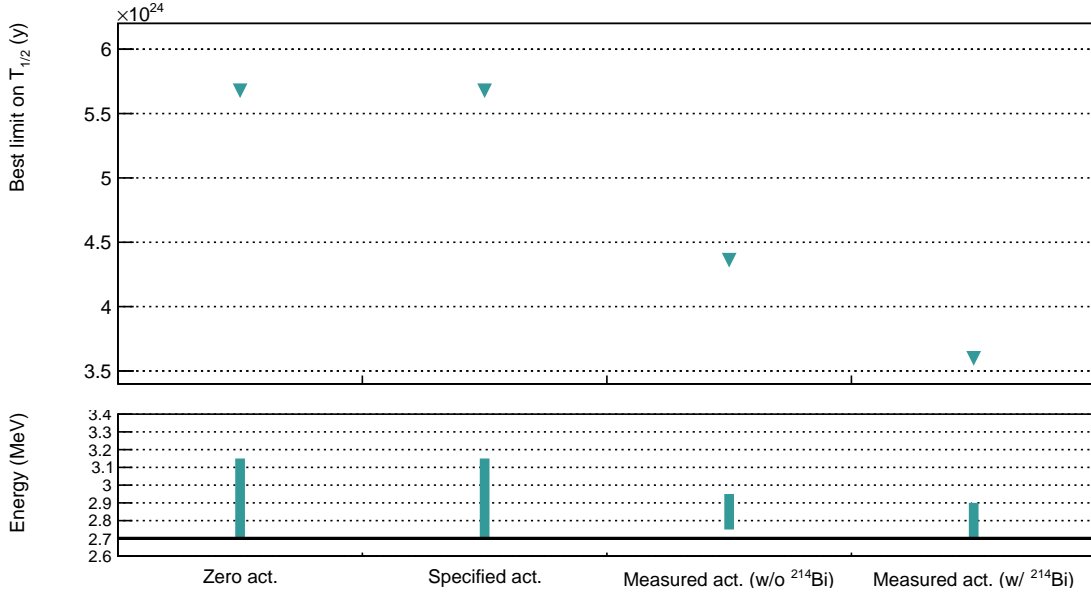


Figure 3.4: The 90% CL limit on the  $0\nu\beta\beta$  half-life (top pad), and the corresponding ROI (bottom pad), as a function of the contamination level considered. For the *zero activities* case, we consider hypothetical contamination levels where  $\mathcal{A}^{\text{Bi}} = \mathcal{A}^{\text{Tl}} = 0$  Bq/kg. The *specified activities* are presented in Tab. 2.3. The *measured activities*, provided by the BiPo detector [11], are presented in the same table. We consider successively a null  $^{214}\text{Bi}$  contamination (*measured act. w/o  $^{214}\text{Bi}$* ), or equals to the  $290\mu\text{Bq/kg}$  upper limit (*measured act. w/  $^{214}\text{Bi}$* ).

Activity ROI	Specified [2.7;3.15] MeV	Measured (w/o $^{214}\text{Bi}$ ) [2.75;2.95] MeV	Measured (w/ $^{214}\text{Bi}$ ) [2.7;2.9] MeV
$\epsilon_{0\nu}$	14.7%	11.3%	14.3%
$2\nu\beta\beta$	0.418	0.122	0.418
$^{208}\text{Tl}$	0.0475	0.688	0.699
$^{214}\text{Bi}$	0.0546	0	1.55
$^{222}\text{Rn}$	0.292	0.173	0.287
Total	0.812	0.983	2.95

Table 3.3: Selection efficiency of  $0\nu\beta\beta$  events and expected number of backgrounds events in the optimised ROI, for the exposure of the SuperNEMO demonstrator (17.5 kg.y). Three levels of contamination are considered.

the statement made on Feldman-Cousins statistics. For the two measured activity cases, the expected number of background events increases significantly, explaining the degradation of the sensitivity. Hopefully, both regions of interest are highly reduced, especially for the case without  $^{214}\text{Bi}$ , where the lower bound is increased from 2.7 to 2.75 MeV. As this 50 keV wide energy region is populated with a non-negligible number of background events, this change in  $E_{\text{min}}$  usefully reduces the  $2\nu\beta\beta$  background contribution, thereby limiting the increase of total expected number of background.

The degradation of the limit on the  $0\nu\beta\beta$  half-life with the level of

contamination remains acceptable. However, we can try improving the situation by exploring new background rejection techniques. This would be especially useful for the final detector case, where a slight increase in internal contaminations could be highly harmful, all the more so as the upper limit given for  $^{214}\text{Bi}$  turns out to be the true contamination level.

### 3.4.2 Optimisation of event selection

Following the BiPo radiopurity measurements, we wish to implement additional event selections, to reject a higher quantity of background. Most of the double beta experiments are only sensitive to the total electron energy sum. The unique SuperNEMO tracko-calo technology confers the experiment the ability to characterise single particles (individual energies, emission angles...). Based on previous studies [9] [24], *topological cuts*, relying on these additional observables, can be set up. They are especially designed to reject events where the two electrons are not emitted simultaneously, or from the same location on the source foils.

#### 3.4.2.1 The internal probability

Based on time-of-flight (TOF) computation, the internal probability ( $P_{int}$ ) is derived from the internal  $\chi^2_{int}$  (see details in Sec. 2.3.3.1). In Fig. 3.5 are presented the internal probability spectra for the  $0\nu\beta\beta$  signal and all background processes, after the first-order selections. These distributions are normalised to the double

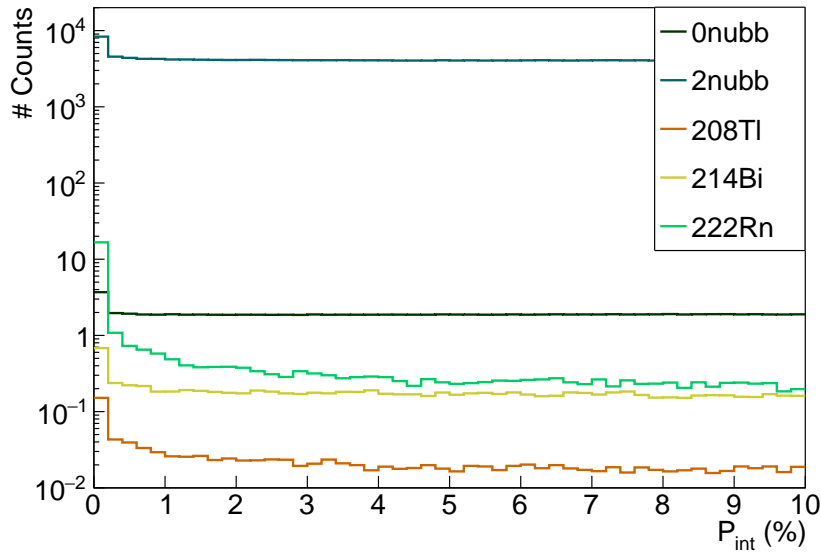


Figure 3.5: Internal probabilities for all processes. First-order cuts have been applied.  $\beta\beta$  distributions are normalised to the half-lives, and background processes are normalised to the specified activities.

beta half-lives, and the nominal activities. Equivalent distributions, but with different  $^{214}\text{Bi}$  and  $^{208}\text{Tl}$  contamination levels, can be derived for the case of measured activities. The internal probability distributions for the  $0\nu\beta\beta$  and  $2\nu\beta\beta$

processes follow the expected flat distribution for electrons emitted simultaneously from the source. As internal Bismuth disintegration actually takes place inside the sources, the  $^{214}\text{Bi}$  distribution is also flat. The same could have been assumed for Thallium, however, the distribution is distorted at low internal probabilities. This might be explained by the existence of a metastable excited state ( $\tau_{1/2} = 294\text{ps}$ ) of the daughter nuclei, which would slightly delay the second electron emitted via internal conversion. This feature is addressed in detail in Chap. 4. The Radon, being a non-internal background, presents a large peak at low internal probabilities.

We want to evaluate the influence of a cut-off on the simulations using internal probability as a rejection criterion: simulated events are selected only if their  $P_{int}$  value is upper than a given limit. The standard value applied in NEMO-3 analyses was  $P_{int} > 4\%$ . We wish to establish the most adequate  $P_{int}$  selection level for the SuperNEMO demonstrator. To do so, we vary the  $P_{int}$  minimal value applied on simulations, and for each we evaluate the limit reached on  $T_{1/2}^{0\nu}$  (at a 90 % confidence interval), as well as the optimised ROI. The best internal probability cut-off value to be applied is the one maximising this sensitivity, and is specific for each contamination level.

We depict in Fig. 3.6 a set of four figures that help to better understand this optimisation. We consider two levels of contamination, the specified and measured contamination levels (taking the upper limit for  $^{214}\text{Bi}$ ). We first detail these figures for the case of the specified activities and then explain what we observe for the measured activities.

**Specified activities** The total expected number of background in the ROI (Fig. 3.6a) is very low compared to one, smaller than 0.8 for  $P_{int} > 0\%$ , and constantly decreases when the minimal cut on  $P_{int}$  increases. Therefore, the number of excluded signal events,  $N_{0\nu}^{\text{excl.}}$ , is set to its minimal value of 2.303, regardless of the  $P_{int}$  level. As a consequence, the ROI bounds are stable (Fig. 3.6b). As the ROI do not influence the selection efficiencies,  $\epsilon_{0\nu}$  is only impacted by the  $P_{int}$  level applied, and decreases with it (Fig. 3.6c). All these observation allow to understand the evolution of  $T_{1/2}^{0\nu}$  (Fig. 3.6d), decreasing with the  $P_{int}$  level applied on simulations. The sensitivities displayed for a 0% cut-off on  $P_{int}$  of course correspond to the results given in Fig. 3.4.

**Measured activities** The total number of expected background event is, naturally, higher than for the specifications, and above all is greater than the 2.303 limit. Nevertheless, this level is too low for the  $P_{int}$  cut-off to have an impact, and the number of expected background remains constant. When the minimal acceptable  $P_{int}$  is changed from 0 to 1 %, the ROI upper bound increases from 2.9 to 3.05 MeV. Usually, the variation of this bound does not have such a great impact on the event selection. Nevertheless, in the measured activities case, for a  $P_{int} > 0\%$  level, the ROI is optimised at the narrow [2.7;2.9] MeV interval, where the upper bound is located in an energy region still populated by signal (see Fig. 3.4). Therefore, even small variations in this ROI has a great impact on the  $0\nu\beta\beta$  selection efficiency, explaining this local increase. We then observe a slight increase of  $0\nu\beta\beta$  selection efficiency for the level  $P_{int} > 1\%$ . For  $P_{int}$  selections



### 3. SENSITIVITY OF THE SUPERNEMO DEMONSTRATOR TO THE $0\nu\beta\beta$

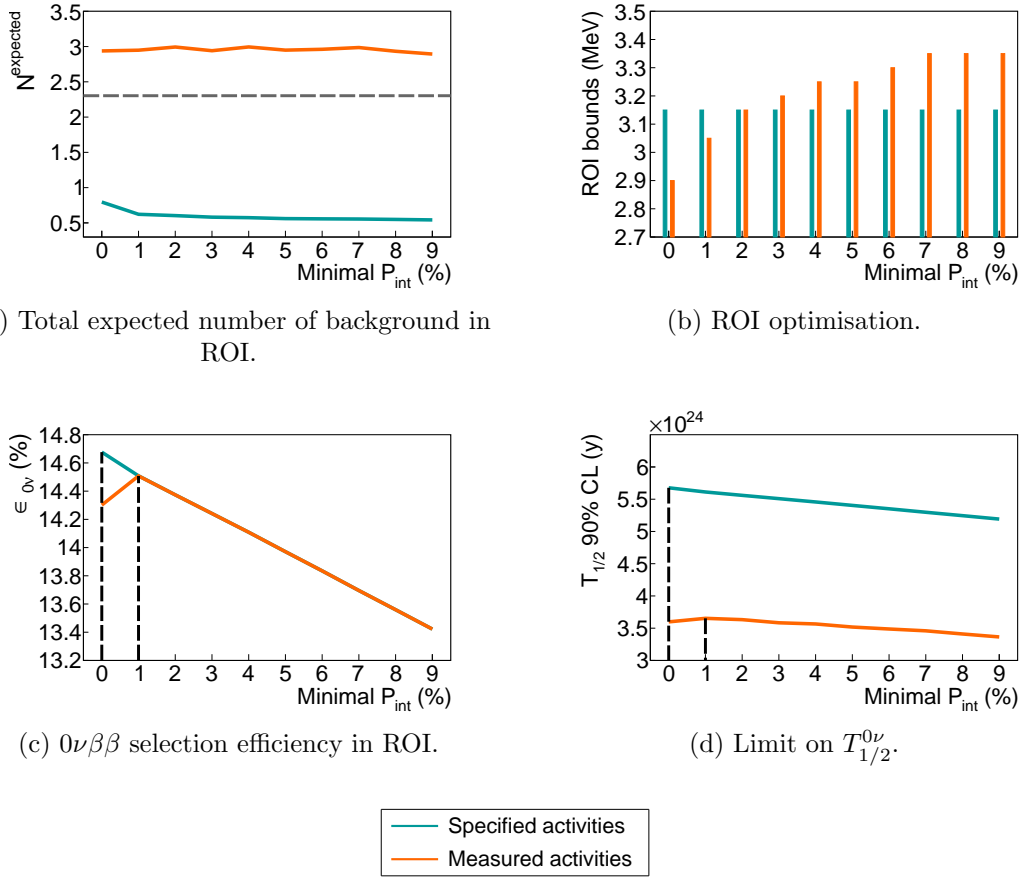


Figure 3.6: Total number of expected background in ROI (a), evolution of the regions of interest (b),  $0\nu\beta\beta$  selection efficiency in ROI (c), and limit set on  $T_{1/2}^{0\nu}$  at 90% CL (d), as a function of the cut-off applied on internal probability,  $P_{\text{int}}$ . The ROI is optimised for each  $P_{\text{int}}$  value. Results are displayed for two contamination levels: the specified (blue) and the measured (orange) activities (taking into account the upper limit provided for  $^{214}\text{Bi}$ ). An exposure of 17.5 kg.y is considered. Two vertical dashed lines in (c) and (d) display the best  $P_{\text{int}}$  selections to be applied in order to improve the  $T_{1/2}^{0\nu}$  sensitivity of the experiment.

greater than 1 %, we come back in cases where the upper bound of the ROI no longer has an impact on  $\epsilon_{0\nu}$ . At this level, only variations of the total number of background events, showed in Fig. 3.6a have an impact. As the limit set on  $T_{1/2}^{0\nu}$  depends directly on  $\epsilon_{0\nu}$ , the variations presented in Fig. 3.6c fully explain the results displayed in Fig. 3.6d, presenting the evolution of  $T_{1/2}^{0\nu}$  with the internal probability selection level.

The optimisation work we have just presented is of interest in the case of measured activities, where the cut-off on  $P_{\text{int}}$  is set at 1%. We will see in the following sections that this optimisation is also be useful, especially when studying the influence of the magnetic field. However, this rejection criterion has only a limited impact on the improvement of  $T_{1/2}^{0\nu}$  sensitivity for the specified activities, because of the very low contamination levels considered. Indeed, paradoxically, the selection on internal probability worth it only if there is enough background



events to be rejected, as we can start observing for the measured activities case. Nevertheless, in that case, we recommend to keep at least a loose cut-off at  $P_{int} > 4\%$ . Indeed, this only slightly degrades the sensitivity (around 4%) while insuring the rejection of potential harmful external backgrounds for a more general study.

### 3.4.2.2 Vertices distance

NEMO-3 analyses also used the distance between the reconstructed vertices on the source foils as a background rejection criterion. As we have shown that the additional  $P_{int}$  cut-off is poorly adapted for the low activities of SuperNEMO sources, it is interesting to know if we can improve the results by using this second selection. Thanks to the trajectory fitting algorithm, we have access to the  $(Y, Z)$  coordinates of the latter, and by extension, to the distance between them. In the previous studies, the choice was made to look at the effect of this selection, separately on the  $Y$  (perpendicular to the wires) and  $Z$  (parallel to the wires) directions. We choose to follow the same approach, and we give the results for a cut along the  $Z$  axis, but the conclusions would remain valid for the  $Y$  direction. Fig. 3.7 shows the distributions of the absolute value of the distance between foil vertices for each process studied. We would use this information in order

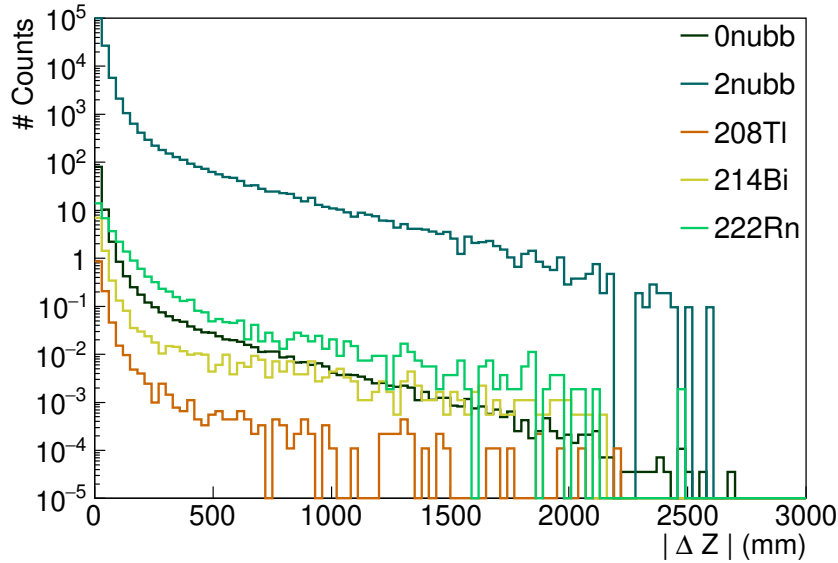


Figure 3.7: Distance along the  $Z$  direction between the vertices of the 2 reconstructed electrons, for each process considered. The  $2\nu\beta\beta$  spectrum is normalised to  $T_{1/2}^{2\nu} = 9.39 \times 10^{19}$  y, and  $^{208}\text{Tl}$ ,  $^{214}\text{Bi}$  and  $^{222}\text{Rn}$  backgrounds are normalised to the nominal activities. The amplitude of the  $0\nu\beta\beta$  is arbitrarily set at the 90% limit obtained with NEMO-3. No energy cut is applied.

to maximise the double  $\beta$  decays to be selected, while rejecting natural isotope disintegrations.

In the same way as the previous paragraph, Fig. 3.8 displays all informations leading to the maximisation of  $T_{1/2}^{0\nu}$ , allowing to study the impact of the vertices

### 3. SENSITIVITY OF THE SUPERNEMO DEMONSTRATOR TO THE $0\nu\beta\beta$

distance cut-off on the final sensitivity. Overall, these figures show us that too strict

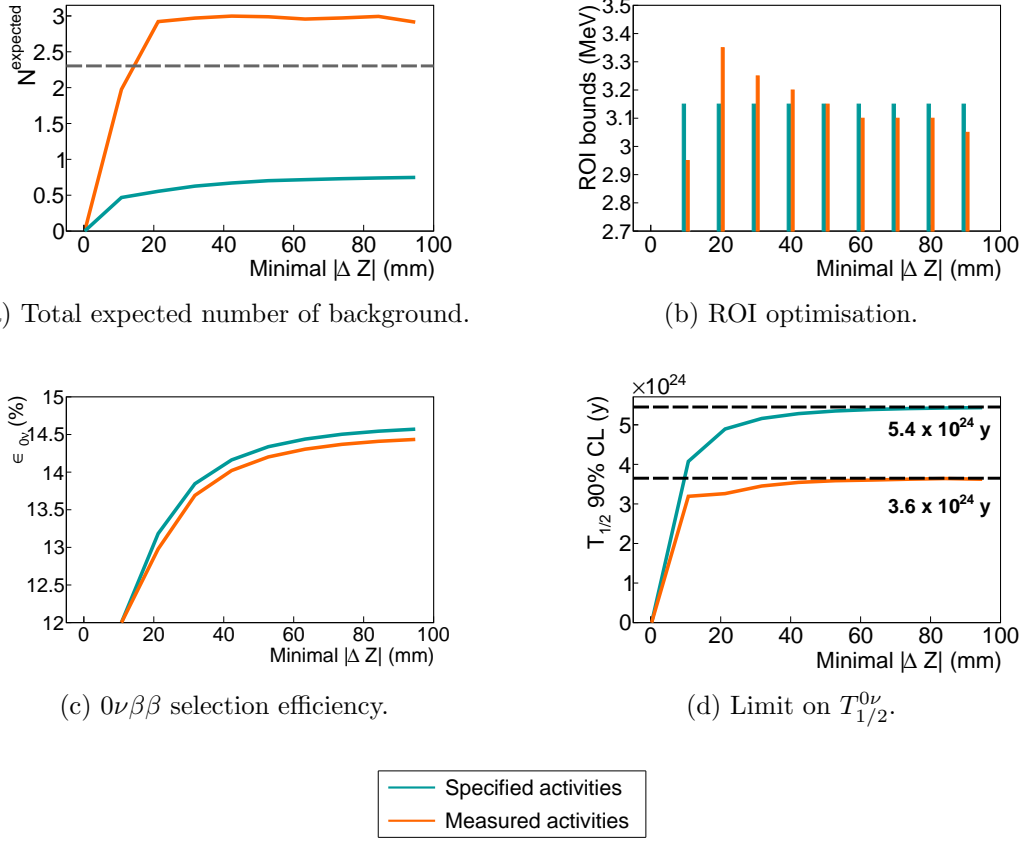


Figure 3.8: Total number of expected background in ROI (a), evolution of the regions of interest (b),  $0\nu\beta\beta$  selection efficiency in ROI (c), and limit set on  $T_{1/2}^{0\nu}$  at 90% CL (d), as a function of the cut-off applied on distance between vertices,  $|\Delta Z|$ . The ROI is optimised for each  $|\Delta Z|$  cut. Results are displayed for two contamination levels: the specified (blue) and the measured (orange) activities (taking into account the upper limit provided for  $^{214}\text{Bi}$ ). An exposure of 17.5 kg.y is considered.

cut-off on the distance between vertices would lead to a decrease in sensitivity. Because of the variations of the  $0\nu\beta\beta$  selection efficiency and the total number of background events, the  $T_{1/2}^{0\nu}$  distributions reaches a plateau, corresponding to the sensitivities achieved with the first-order cuts and optimised  $P_{\text{int}}$ . In practice, as it is done for  $P_{\text{int}}$ , a selection on vertex distance will always be applied, even if it is very loose, as such a cut-off could be useful for rejecting unexpected background (coincidence between independent events, for instance). We recommend to apply a loose cut-off level at  $|\Delta Z| < 80$  mm, which does not degrade significantly the sensitivity. The same conclusions apply to the  $|\Delta Y|$  cut-off.

The idea of having implemented these two selections (on the internal probability and on the distance between vertices) comes from a previous NEMO-3 analysis on the background rejection. For the SuperNEMO demonstrator case, the levels of contaminations we are dealing with is remarkably low for most of the topological

cut-offs to be worth applying. However, in practice, applying loose topological selections on the data remains necessary, especially to reject external background events. The minimal cut-off level to be applied is  $P_{int} > 4\%$  and  $|\Delta Z| < 80$  mm (similarly for  $|\Delta Y|$ ), and can be optimised by taking into account the sources activity.

For future studies, it is useful to give the efficiencies of these loose selections, for the signal and for each background considered (Tab. 3.4a), as well as the expected number of background in the ROI (Tab. 3.4b). As detailed, regions of

Cut-off	First-order cuts (%)	Internal probability (%) $P_{int} > 4\%$	Vertex distance (%) $ \Delta Z  < 80$ mm
$0\nu\beta\beta$	26.9	25.3	24.7
$2\nu\beta\beta$	9.15	8.56	8.21
$^{208}\text{Tl}$	0.106	0.0889	0.0846
$^{214}\text{Bi}$	0.168	0.151	0.144
$^{222}\text{Rn}$	0.0177	$7.91 \times 10^{-3}$	$5.34 \times 10^{-3}$

(a) Selection efficiencies for the three levels of selection (first-order,  $P_{int}$  and vertex distance), in the full energy range.

Activity	Specified		Measured (w/ $^{214}\text{Bi}$ )	
Cut-off ROI (MeV)	$P_{int} > 4\%$ [2.7;3.15]	$ \Delta Z  < 80$ mm [2.7;3.15]	$P_{int} > 4\%$ [2.7;3.25]	$ \Delta Z  < 80$ mm [2.7;3.3]
$\epsilon_{0\nu}$	14.1%	13.9%	14.1%	13.9%
$2\nu\beta\beta$	0.392	0.383	0.392	0.383
$^{208}\text{Tl}$	0.0338	0.0323	1.08	1.09
$^{214}\text{Bi}$	0.0491	0.0491	1.42	1.42
$^{222}\text{Rn}$	0.115	0.0782	0.115	0.0782
Total	0.590	0.543	3.01	2.97

(b) Selection efficiency of  $0\nu\beta\beta$  events and expected number of backgrounds events in the optimised ROI, for the exposure of the SuperNEMO demonstrator (17.5 kg.y), for successive application of topological selections. Specified and measured activities (taking into account the upper limit for  $^{214}\text{Bi}$  contamination) are considered.

Table 3.4: The selection efficiencies and expected number of background events for the topological selections.

interest are optimised for each selection. The selection efficiencies show topological cuts have a huge impact on Radon selection, as they are especially designed to reject non-internal events. The  $P_{int}$  cut-off is also efficient in rejecting Thallium internal events, because of the existence of a metastable excited state, described earlier. A special technique to reject efficiently  $^{208}\text{Tl}$  background is also addressed in Chapter 4.

After the topological cut-off optimisation, the SuperNEMO demonstrator would reach a sensitivity of  $T_{1/2}^{0\nu} > 5.4 \times 10^{24}$  y if specified activities are reached, corresponding to the effective neutrino mass range  $\langle m_{\beta\beta} \rangle < [0.25 - 0.48]$  eV. For the measured activities, supposing  $^{214}\text{Bi}$  activity reaches the measured upper limit,  $T_{1/2}^{0\nu} > 3.6 \times 10^{24}$  y and  $\langle m_{\beta\beta} \rangle < [0.31 - 0.59]$  eV.

In the following we review the influence of the 25 Gauss magnetic field inside the detector on the sensitivity reachable by the SuperNEMO demonstrator.

## 3.5 Impact of the magnetic field on the sensitivity

The SuperNEMO demonstrator was originally designed with a copper coil, similarly to NEMO-3, delivering a magnetic field inside the tracker volume. This 25 Gauss magnetic field is high enough to bend the trajectory of the few MeV electrons and positrons of interest for SuperNEMO, without too strongly preventing them from reaching the calorimeter. In practice, this magnetic field is mainly used to identify and reject the electron-positron pairs created by high energy  $\gamma$ 's, themselves emitted after a neutron capture. However, as explained in sub-section 3.1.3, we choose to not consider the contribution of this external background for this study's background model. We therefore focus on evaluating the influence of the presence of the magnetic field on the rejection of natural isotopes contaminating the source foils and wire chamber.

### 3.5.1 Simulations of the magnetic field inside the demonstrator and reconstructed track fit

In order to study the influence of the magnetic field on the demonstrator sensitivity to the  $0\nu\beta\beta$  decay, the simulations and reconstructions of signal and backgrounds have been performed in two different conditions.

- Simulations with a uniform 25 Gauss magnetic field (following recommendations [9]). Results about the final sensitivity achieved in this condition have already been presented earlier in this chapter. The possible variations of the field intensity, mainly due to the calorimeter magnetic shields, are not taken into account for these simulations. This will be discussed in sub-section 3.5.4.
- Simulations where the magnetic field is turned off.

Each magnetic field condition has the same number of simulated events, as summed up in Tab. 3.1.

Depending on the case under consideration, the charged particles do not have the same trajectory curvature. In the first uniform on-field case, they are bended. The track fit algorithm then performs two distinct trajectory fittings: one with a helix and one with a line. The most accurate fit is chosen and provides information on the charge of the detected particle. In the second off-field case, the fitting algorithm is modified to match line trajectories.

### 3.5.2 Impact of the magnetic field on signal and background selections

Among first-order event selection criteria considered in Sec. 3.2, the one on the trajectory curvature is of primary importance with regard to the influence of the magnetic field on the final sensitivity. Indeed, when the magnetic field is switched on, the charged particles of few MeV (as electrons and positrons) have curved trajectories. A particle is then identified as an electron when the trajectory fitting results in a negative curvature. When the magnetic field is switched off, the trajectory of the charged particles takes place in a straight line<sup>4</sup>. This last selection criterion on the track curvature is then no longer applied.

Consequently, the number of identified  $2e$  topologies selected by the first-order cuts is increased for the off-field case. To illustrate this effect, we give in Tab. 3.5 the selection efficiencies of signal and background in the total energy range  $[0;4]$  MeV, for the two cases of magnetic field. The  $0\nu\beta\beta$  efficiency increases,

Field	On	Off
$0\nu\beta\beta$	26.9	31.4
$2\nu\beta\beta$	9.16	10.6
$^{208}\text{Tl}$	0.106	0.169
$^{214}\text{Bi}$	0.168	0.252
$^{222}\text{Rn}$	0.0177	0.0924

Table 3.5: Selection efficiencies (%) in the full energy range  $[0;4]$  MeV, for on and off-field cases. First-order cut-offs have been applied.

but also the efficiency of background selection. In particular, the Radon efficiency increases very significantly. Indeed, in some cases, the two electrons resulting from the decay of Bismuth on the tracker wires can be emitted back to back. One of the two electrons can subsequently pass through the source in the direction of the opposite calorimeter. When this decay takes place close to the source, it is arduous to reconstruct a helix in the presence of a magnetic field, and this type of event is easily rejected. Whereas without a field there is no selection of curvature so these events are more likely to be selected.

However only variations of selection efficiencies in the ROI, between on-field and off-field cases, are the source of modifications on the final sensitivity. We present these in Tab. 3.6 for the two field cases. The selection efficiencies of  $\beta\beta$  decays are disadvantaged by the lower bound of the ROI for the off-field case. The slight variation of the ROI upper bound have a measurable impact on the expected number of  $^{208}\text{Tl}$  events, as this background has a contribution at high energies. The increase of  $^{222}\text{Rn}$  events, despite the ROI lower bound variation, is directly explained by the phenomenon, described above, of selecting  $2e$  events issued back to back close to the source. As expected, these observations result in a decrease in sensitivity when the field is switched off, giving

$$T_{1/2}^{0\nu} > 4.8 \times 10^{24} \text{ y} \quad (90\% \text{CL}) \text{ (off-field)}. \quad (3.10)$$

<sup>4</sup>In saying this, we do not take into account possible deviations in the trajectory of the particles, due in particular to multiple scattering in the tracker.

### 3. SENSITIVITY OF THE SUPERNEMO DEMONSTRATOR TO THE $0\nu\beta\beta$

Field	On [2.7;3.15] MeV	Off [2.75;3.2] MeV
$\epsilon_{0\nu}$	14.7%	12.4%
$2\nu\beta\beta$	0.418	0.0353
$^{208}\text{Tl}$	0.0475	0.0600
$^{214}\text{Bi}$	0.0546	0.0452
$^{222}\text{Rn}$	0.292	0.553
Total	0.812	0.693

Table 3.6: Selection efficiency of  $0\nu\beta\beta$  events and expected number of backgrounds events in the optimised ROI, for the exposure of the SuperNEMO demonstrator (17.5 kg.y). Specified activities are considered. The two on- and off-field cases are compared. First-order cut-offs have been applied.

As concluded in Sec. 3.4, topological selections are especially efficient in rejecting the Radon background. Therefore, the application of these additional cut-offs, for the off-field case, could be interesting, in order to increase the sensitivity. Following the work presented in the previous section, we optimise these selections for the particular off-field case, both for the specified and measured contamination levels<sup>5</sup>. Fig. 3.9 summarises the results obtained in sensitivity before and after application of these topological cut-offs. The left part of the panel gives information on the evolution of sensitivity, when only the first-order cut-offs are applied. We come back to the conclusions given above: when the magnetic field is switched-off, we lose sensitivity, regardless of the level of contamination considered. On the right side of the figure, we present the results when the topological cuts are applied. For the on-field case, the addition of these selections have almost no effect on the sensitivity, as concluded in sub-section 3.4.2. However, as predicted, we are beginning to see the usefulness of these selections in the off-field case, as a higher number of  $^{208}\text{Tl}$  and  $^{222}\text{Rn}$  events passed the first-order selections. For instance, for the specification case,  $T_{1/2}^{0\nu}$  goes from  $4.8 \times 10^{24}$  y to  $6.1 \times 10^{24}$  y, an improvement of  $\sim 30\%$ .

In Tab. 3.7 are presented the expected number of background events in the ROI for the off-field condition, before and after application of topological cut-offs, for the specified and measured activities (taking into account the upper limit for the  $^{214}\text{Bi}$  contamination). This selection allows to reject mainly  $^{222}\text{Rn}$  background. Prior to the application of the topological cuts, the relatively large number of Radon events (0.553) prevented the value of the lower limit of ROI from lowering. Once the topological cuts have drastically reduced Radon, the lower limit decreases, thus increasing the  $2\nu\beta\beta$ . Fortunately, it is also accompanied by an increase in the selection of  $0\nu\beta\beta$  events. Finally, even if the absence of the magnetic field has the effect of reducing the sensitivity to the  $0\nu\beta\beta$  decay, topological cuts allow this effect to be compensated for, making it possible to reach higher values of  $T_{1/2}^{0\nu}$ .

<sup>5</sup>As done in sub-section 3.4.2, for the Bismuth measured contamination, we consider here the upper limit where  $\mathcal{A}^{\text{Bi}} = 290 \mu\text{Bq/kg}$ .

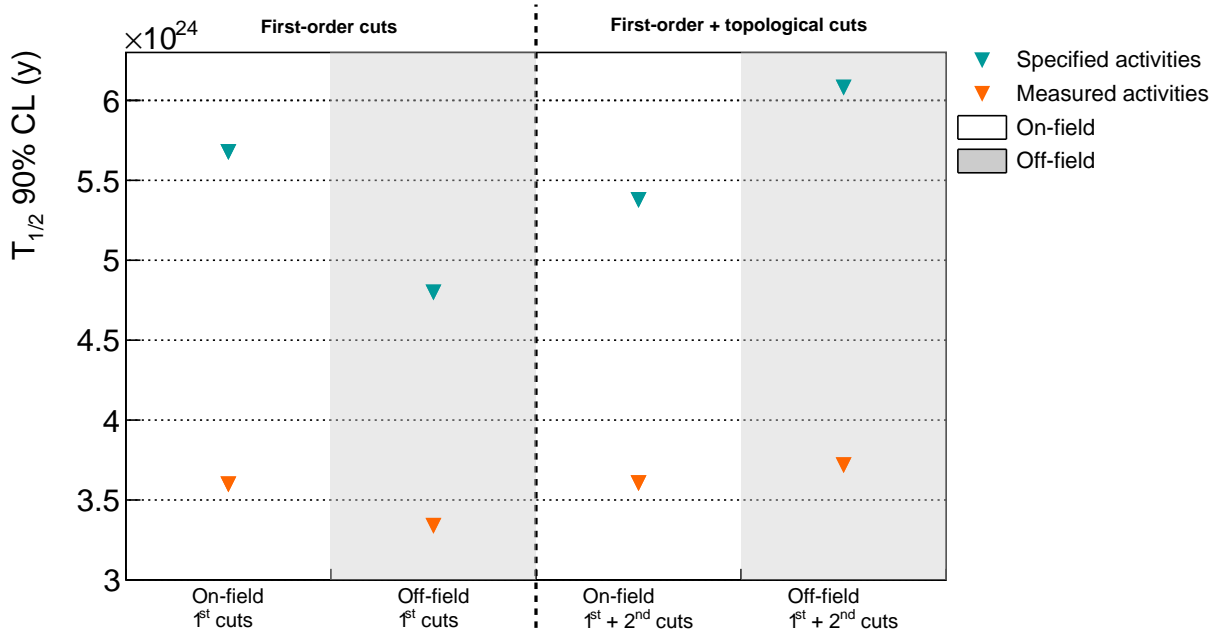


Figure 3.9:  $T_{1/2}^{0\nu}$  (90% CL) considering various conditions: on- and off-field (white and grey stripes), first-order and addition of topological cut-offs (left/right parts of the panel), specified and measured activities (blue and orange triangle markers). The measured activities are  $\mathcal{A}^{\text{Tl}} = 54 \mu\text{Bq/kg}$ ,  $\mathcal{A}^{\text{Bi}} = 290 \mu\text{Bq/kg}$  and  $\mathcal{A}^{\text{Rn}} = 0.15 \text{ mBq/m}^3$ .

Activity	Specified		Measured (w/ $^{214}\text{Bi}$ )	
Cut-off ROI (MeV)	First-order [2.75;3.2]	Topological [2.7;3.2]	First-order [2.65;2.9]	Topological [2.7;2.9]
$\epsilon_{0\nu}$	12.4%	15.7%	19.1%	14.8%
$2\nu\beta\beta$	0.0353	0.453	1.56	0.440
$^{208}\text{Tl}$	0.0600	0.0506	1.01	0.613
$^{214}\text{Bi}$	0.0452	0.0706	2.94	1.84
$^{222}\text{Rn}$	0.553	0.0894	1.42	0.0689
Total	0.693	0.664	6.93	2.96

Table 3.7: Selection efficiency of  $0\nu\beta\beta$  events and expected number of backgrounds events in the optimised ROI, for the exposure of the SuperNEMO demonstrator (17.5 kg.y), with off-field condition. Specified and measured (with  $^{214}\text{Bi}$ ) activities are considered. Topological cut-offs are optimised:  $P_{\text{int}} > 1\%$  and  $|\Delta Z| < 80\text{mm}$  (specified activities),  $P_{\text{int}} > 5\%$  and  $|\Delta Z| < 80\text{mm}$  (measured activities)

### 3.5.3 Influence of the magnetic field on optical modules and reconstruction efficiency

In the previous sub-section, a comparative study has been led to evaluate the influence of the presence of a magnetic field on the event selection, and thus on the final sensitivity. However, as things stand now, some features of the



demonstrator are not yet implemented in the simulation software, and could have a great impact on the results presented above. In particular, studies have been led by the collaboration to evaluate the influence a 25 Gauss magnetic field on the optical modules, as well as on the event reconstruction [9][10].

SuperNEMO PMTs are protected from the external magnetic field by individual iron shields. Unfortunately, the latter do not perfectly protect the PMTs, and a residual magnetic field is measured inside the shieldings, leading to losses in charge collected by PMTs close to 8%. This study also revealed the energy resolution would be worsened with a relative decrease of 3% of the initial value of 8% at 1 MeV. Moreover, the PMTs shieldings could themselves severely impact the shape of the field lines, as well as its intensity. In fact, with a 25 Gauss magnetic field generated by the copper coil, the magnetic shields are responsible for the field strength decreasing, and barely 10 G is expected near the source foils. Worse, the magnetic field strength decreases very quickly as we get closer to the calorimeter walls, where nearly 0 G could be expected. The reconstruction efficiency could therefore be greatly impacted: the magnetic field intensity varying from the source foils to the calorimeter wall, electrons trajectory curvatures are not constant, and the track-fitting algorithm is less performing. An incorrect description of the distribution of the magnetic field would more strongly impact low-energy electrons.

In the light of these conclusions, it could be interesting to study the evolution of the sensitivity, considering field simulations with more realistic variations inside the detector.

### 3.5.4 Simulations with a non-uniform magnetic field

Simulations with a 25 Gauss *mapped* magnetic field have been performed, taking into account more realistic variations of the field inside the detector [25]. In this condition, the fitting algorithm follows the same steps as for on-field: a helix and linear fit are performed for each simulated event, and the most accurate is selected. Unfortunately, Radon isotope decays could not be simulated with this magnetic field configuration. Indeed, as it is present in the entire wire chamber, simulations would have required too many additional storing resources. Thus, strong conclusions on the sensitivity can't be given. However, it is possible to assess the selection efficiencies of the different processes, and then get an idea of the influence of realistic variations of the field on the final results. Tab. 3.8 compares the selection efficiencies, for the three field cases (uniform on-field, mapped field and off-field), in the total energy range [0;4] MeV. The mapped field case has lower selection efficiencies, compared with uniform field simulations. As announced in the previous sub-section, the magnetic shields distort the field intensity across the detector. Therefore, the fitting algorithm is less efficient in identifying particles with a negative curvature inside the tracker, hence the number of selected  $2e$  topologies is decreased.

Tab. 3.9 presents the expected number of background events in the energy range [2.7;3.2] MeV, for simulations using the realistic mapped field. As expected, the  $0\nu\beta\beta$  selection efficiency is drastically decreased compared with the on-field



Field $P_{int}$	On $P_{int} > 4\%$	Off $P_{int} > 1\%$	Mapped $P_{int} > 4\%$
$0\nu\beta\beta$	24.7	29.3	19.1
$2\nu\beta\beta$	8.21	9.93	6.39
$^{208}\text{Tl}$	0.0846	0.140	0.0774
$^{214}\text{Bi}$	0.144	0.211	0.125

Table 3.8: Signal and background selection efficiencies of on-field, off-field and mapped-field cases, in the energy range [0;4] MeV. The first-order and optimised topological cut-offs have been applied. Especially, for all field conditions,  $|\Delta Z| < 80$  mm.

	Mapped field
$\epsilon_{0\nu}$	10.4%
$2\nu\beta\beta$	0.245
$^{208}\text{Tl}$	0.0279
$^{214}\text{Bi}$	0.0535
Total	0.326

Table 3.9: Selection efficiency of  $0\nu\beta\beta$  events and expected number of background events in the [2.7;3.2] MeV optimised ROI, for the exposure of the SuperNEMO demonstrator (17.5 kg.y), for mapped field simulations. The specified background activities are considered. First-order and optimised topological cuts have been applied ( $P_{int} > 4\%$  and  $|\Delta Z| < 80$  mm).

case, as well as the expected number of background events. As explained above, the selection on track curvature is still applied in this case, and the non-uniform magnetic field causes deviations in the particles trajectory, which are therefore more difficult to identify as electrons. Even if Radon simulation with such field conditions are unavailable, it is interesting to provide an order of magnitude of the  $T_{1/2}^{0\nu}$  limit set with these realistic variations of the field. To do so, we extrapolate the expected number of Radon events in the [2.7;3.2] MeV energy range, from the  $^{214}\text{Bi}$  one. Indeed, we postulate the ratio between these two numbers remain a constant, and the on-field simulations give  $N_{\text{Bi}}/N_{\text{Rn}} \sim 5$ . Taking this into consideration, a limit of  $T_{1/2}^{0\nu} > 4 \times 10^{24}$  y (90 % CL) would be reached with the demonstrator, a  $\sim 30$  % decrease compared with the non-realistic uniform case. This approximation should be examined with caution, however, as magnetic field conditions can greatly influence the selection of Radon and Bismuth events. To be specific, we have seen in Sec. 3.5.2 that between off-field and on-field conditions, the Radon and Bismuth efficiencies varied differently. So, to ensure that our approximation is valid, a more proper study would have to be made. In particular, it would be necessary to study how events where the two electrons are emitted back to back from a wire of the tracker when the field is no longer uniform are treated.

### 3.6 Searching for the Neodymium-150 $0\nu\beta\beta$ decay

This study was conducted jointly with the PhD student Axel Pin, from CENBG [26]. Although we both worked on the whole of the analysis, I presented in detail, in the previous sections, the results regarding the influence of the magnetic field. Meanwhile, Axel Pin presents the possibility of changing the Selenium material by other  $\beta\beta$  isotopes. Indeed, on the model of the NEMO-3 detector, which housed, among others, 6.914 kg of  $^{100}\text{Mo}$  and 0.932 kg of  $^{82}\text{Se}$ , the SuperNEMO detector possesses the technical possibility of exchanging the source material and study several  $\beta\beta$  isotopes. Notably, in the case SuperNEMO demonstrates the feasibility of a large-scale tracko-calorimeter experiment, it would be natural to evaluate the sensitivity of SuperNEMO to the  $0\nu\beta\beta$  decay of other isotopes than  $^{82}\text{Se}$ .

#### 3.6.1 Searching for the $0\nu\beta\beta$ of other isotopes

One of the distinctive features of NEMO detectors is the gaseous detector, designed to track charged particles. Unluckily, this advantage is also a great inconvenience when it comes to Radon contamination. Indeed, Radon enters by diffusion or emanates from the detector materials. It is then interesting to consider  $\beta\beta$  candidates with an energy transition value above the  $Q_\beta = 3.27$  MeV of  $^{214}\text{Bi}$ , a Radon daughter. Another useful criterion is the natural isotopic abundance: typically, considering only isotopic abundances greater than 2% is a reliable basis when selecting potential  $\beta\beta$  emitters. Two nuclei satisfy these two criteria:  $^{96}\text{Zr}$  and  $^{150}\text{Nd}$  (with respective  $Q_{\beta\beta}$  values of 3.35 and 3.36 MeV, and respective isotopic abundances of 2.8 and 5.6 % [27]). As the  $^{150}\text{Nd}$  isotope has the highest  $Q_{\beta\beta}$  value, the current section focuses on evaluating the SuperNEMO sensitivity to the  $0\nu\beta\beta$  decay of this isotope, supposing we have several kg at our disposal. Moreover, the  $^{150}\text{Nd}$  has a more favourable phase space than the  $^{82}\text{Se}$ , on which the half-life limit directly depends.

#### 3.6.2 Sensitivity to the $0\nu\beta\beta$ of $^{150}\text{Nd}$

Until recently, Neodymium was not enrichable in large quantities. Recent developments have resulted in the production of several grams of enriched Neodymium, making this  $\beta\beta$  isotope interesting for the search for  $0\nu\beta\beta$ . Thanks to that, NEMO-3 had available 36.6 g of  $^{150}\text{Nd}$  which were recovered by the collaboration, for a possible reuse for SuperNEMO. The best limit for the search for neutrinoless double  $\beta$  decay of  $^{150}\text{Nd}$  was reached by the NEMO-3 detector with 5.25 years of data acquisition. The detector achieved  $T_{1/2}^{0\nu} > 2.0 \times 10^{23}$  y (90 % CL), corresponding to a range on the effective neutrino mass of  $\langle m_{\beta\beta} \rangle < [1.6 - 5.3]$  eV. The collaboration also measured the  $2\nu\beta\beta$  half-life, with  $T_{1/2}^{2\nu} = [9.34 \pm 0.22 \text{ (stat.)} \pm 0.62 \text{ (syst.)}] \times 10^{18}$  y [28].

We wish to determine the limit on the  $0\nu\beta\beta$  of the  $^{150}\text{Nd}$  that could be reached with the SuperNEMO demonstrator, with an exposure of 17.5 kg.y. We lead this

study considering the activities specified for the  $^{82}\text{Se}$  sources are reached. We use simulations with the 25 Gauss uniform magnetic field. Fig. 3.10 depicts the normalised energy distributions for the  $2e$  topologies selected after application of first-order and topological selections. Signal and background selection efficiencies

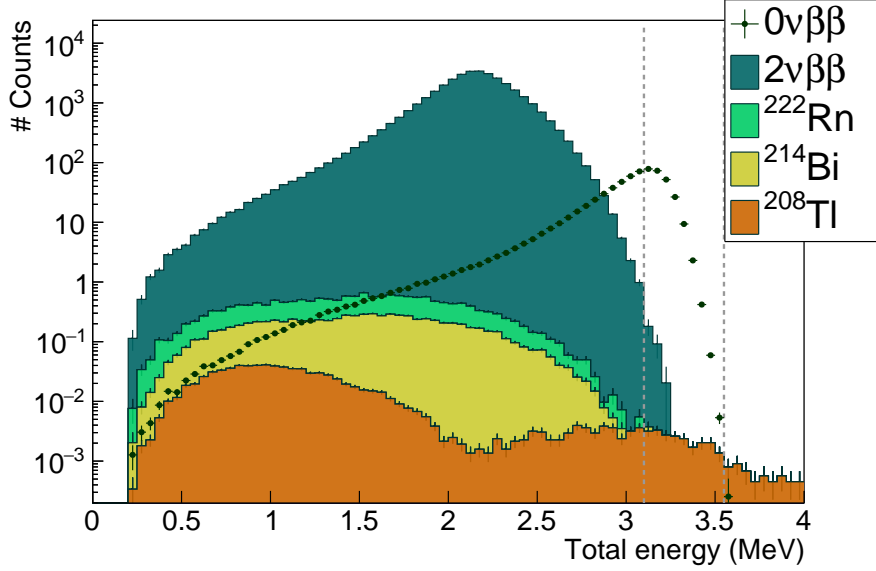


Figure 3.10: Total energy spectra for the  $0\nu\beta\beta$  signal and main backgrounds, for  $^{150}\text{Nd}$  sources and for a 17.5 kg.y exposure. The  $2\nu\beta\beta$  spectrum is normalised to  $T_{1/2}^{2\nu} = 9.34 \times 10^{18}$  y, and  $^{208}\text{Tl}$ ,  $^{214}\text{Bi}$  and  $^{222}\text{Rn}$  backgrounds are normalised to the nominal activities. The amplitude of the  $0\nu\beta\beta$  is arbitrarily set at the limit obtained with NEMO-3  $T_{1/2}^{0\nu} = 2.0 \times 10^{23}$  y. First-order and optimised topological cuts have been applied. The ROI of [3.1;3.55] MeV is depicted by two vertical dashed lines.

for  $^{150}\text{Nd}$  sources, in the total energy range, are given in Tab. 3.10. The selection

Isotope	Selenium	Neodymium
$0\nu\beta\beta$	25.8	25.5
$2\nu\beta\beta$	8.21	8.11
$^{208}\text{Tl}$	0.0846	0.0749
$^{214}\text{Bi}$	0.144	0.138
$^{222}\text{Rn}$	$5.34 \times 10^{-3}$	$5.34 \times 10^{-3}$

Table 3.10: Selection efficiencies in the full energy range [0;4] MeV, for  $^{82}\text{Se}$  and  $^{150}\text{Nd}$  sources. First-order and optimised topological cuts have been applied.

efficiencies of backgrounds are lower for  $^{150}\text{Nd}$  sources than for  $^{82}\text{Se}$  sources. In both cases, for the total energy range the background contribution is dominated by the  $2\nu\beta\beta$  decay. This is caused by the more elevated number of protons in the Neodymium nucleus which induces a stronger Coulombian effect. Indeed, the more the  $\beta\beta$  emitter has a high atomic number  $Z$ , the more the electrons emitted from

inside the source (or passing through it) are likely to interact electromagnetically with it. Despite this, for reasons of limited storage resources, we choose to consider this effect to be negligible for events outside the source, such as Bismuth disintegrations (from Radon) from the tracker wires. Therefore, we choose to use the Radon simulations already generated for the  $^{82}\text{Se}$  sources study. Clearly, further study would be required to ensure that this consideration is reasonable.

In Tab. 3.11 we give the expected number of background events in the optimised ROI [3.1;3.55] MeV. The selection efficiency of the  $0\nu\beta\beta$  decay in this energy range

Isotope ROI	Selenium [2.7;3.15] MeV	Neodymium [3.1;3.55] MeV
$\epsilon_{0\nu}$	14.4%	10.3%
$2\nu\beta\beta$	0.39	0.28
$^{208}\text{Tl}$	0.044	0.029
$^{214}\text{Bi}$	0.053	$5.6 \times 10^{-4}$
$^{222}\text{Rn}$	0.20	0.0
Total	0.687	0.309

Table 3.11: Selection efficiency of  $0\nu\beta\beta$  events and expected number of backgrounds events in the optimised ROI, for the exposure of the SuperNEMO demonstrator (17.5 kg.y), for  $^{82}\text{Se}$  and  $^{150}\text{Nd}$  sources. The specified background activities are considered. First-order and optimised topological cuts have been applied.

is also given. Although the  $2\nu\beta\beta$  half-life of the  $^{150}\text{Nd}$  is lower than that of the  $^{82}\text{Se}$  by a factor  $\sim 10$ , the number of  $2\nu\beta\beta$  events in the ROI remains low. Indeed, thanks to the Coulombian effects described above, this process has a limited contribution at high energy. The high energy of transition  $Q_{\beta\beta} = 3.36$  MeV of  $^{150}\text{Nd}$  implies that the contributions of  $^{214}\text{Bi}$  and  $^{222}\text{Rn}$  are very small, or even zero. The  $2\nu\beta\beta$  and  $^{208}\text{Tl}$  events are therefore the major contributors to the background. Consequently, if the choice of changing the source material with  $^{150}\text{Nd}$  isotope was made, it would be conceivable to release the specifications on  $^{214}\text{Bi}$  and  $^{222}\text{Rn}$  backgrounds.

The SuperNEMO demonstrator, with 7 kg of  $^{150}\text{Nd}$  and 2.5 years of data acquisition, would achieve a  $T_{1/2}^{0\nu} > 2.2 \times 10^{24}$  y sensitivity, one order of magnitude higher than the best limit ever reached. The corresponding limit on the effective neutrino mass is  $\langle m_{\beta\beta} \rangle = [0.15 - 0.50]$  eV. This is a better result than for  $^{82}\text{Se}$  sources, as the  $^{150}\text{Nd}$  has a more favourable space factor.

### 3.7 The final detector sensitivity

The ultimate goal of the SuperNEMO demonstrator is to show that the NEMO technology is scalable to probe unprecedented half-life on the  $0\nu\beta\beta$  decay. The final detector would consist in building 20 modules similar to the demonstrator. In this context, we estimate the final detector sensitivity to the  $0\nu\beta\beta$  decay.

We suppose the specified activities of  $\mathcal{A}^{\text{Tl}} = 2 \mu\text{Bq/kg}$ ,  $\mathcal{A}^{\text{Bi}} = 10 \mu\text{Bq/kg}$  and  $\mathcal{A}^{\text{Rn}} = 0.15 \text{ mBq/m}^3$  are reached. The simulations with an uniform magnetic field are used.

Tab. 3.12 shows the number of expected events in the optimised ROI for first-order and topological cut-offs. The total expected number of background events

Cut ROI	First-order [2.75;2.95] MeV	Topological [2.75;3.1] MeV
$\epsilon_{0\nu}$	11.3%	10.7%
$2\nu\beta\beta$	3.48	3.36
$^{208}\text{Tl}$	0.728	0.756
$^{214}\text{Bi}$	0.945	0.835
$^{222}\text{Rn}$	6.93	2.16
Total	12.1	7.11

Table 3.12: Selection efficiency of  $0\nu\beta\beta$  events and expected number of backgrounds events in the optimised ROI, for the exposure of the SuperNEMO final detector (500 kg.y). The specified background activities are considered. The topological selections have been optimised:  $P_{\text{int}} > 4\%$  and  $|\Delta Z| < 80 \text{ mm}$ .

is high enough for the optimised cut-offs to be worth it, with  $P_{\text{int}} > 4 \%$  and  $|\Delta Z| < 80 \text{ mm}$  (similarly for  $|\Delta Y|$ ). They allow primarily to reduce the Radon background by a factor 3. Due to the optimisation of the ROI, especially to the raising of the upper bound, the  $^{208}\text{Tl}$  background is a little increased, without important consequences, as the  $2\nu\beta\beta$  and  $^{222}\text{Rn}$  dominate the total number of background in this energy range.

With an exposure of 500 kg.y, the SuperNEMO final detector should reach a sensitivity of  $T_{1/2}^{0\nu} > 5.4 \times 10^{25} \text{ y}$ , with  $^{82}\text{Se}$  sources, corresponding to  $\langle m_{\beta\beta} \rangle = [0.079 - 0.15] \text{ eV}$ . By comparison, with the same exposure and background specifications but with  $^{150}\text{Nd}$  sources, the final detector would achieve a sensitivity of  $T_{1/2}^{0\nu} > 2.2 \times 10^{25} \text{ y}$ , in the [3.1;3.75] MeV ROI, corresponding to  $\langle m_{\beta\beta} \rangle = [0.046 - 0.15] \text{ eV}$ .

## 3.8 Conclusion

Latest measurements of source activities by BiPo-3 show that the specified background level for Thallium isotope is not reached, although it is improved in average by a factor 2, compared to NEMO-3. An upper limit is given for the internal Bismuth isotope activity. In addition, not all sources were measured and a precise measurement is expected to be provide by the SuperNEMO demonstrator when data acquisition will begin. C-sections measurements with a concentration line showed the Radon targeted activity can be achieved for the demonstrator, with an gas flow rate of  $2 \text{ m}^3/\text{h}$  inside the chamber. Topological selections, designed to reject non-internal and non-simultaneous  $2e$  events, have been optimised, and allowed to reduce the Radon background by a factor 3 for the final demonstrator. Assuming the target background activities are reached,

the SuperNEMO demonstrator, running for two and half years with 7 kg of  $^{82}\text{Se}$ , would be able to set a limit on the  $0\nu\beta\beta$  process  $T_{1/2}^{0\nu} > 5.4 \times 10^{24}$  years, translating into a limit on the neutrino effective mass  $\langle m_{\beta\beta} \rangle < [0.25 - 0.48]$  eV<sup>6</sup>. Taking into account the measured activities (with 290  $\mu\text{Bq/kg}$  of  $^{214}\text{Bi}$ ), the limit on  $T_{1/2}^{0\nu}$  would be decreased by a factor 33% with  $T_{1/2}^{0\nu} > 3.6 \times 10^{24}$  years ( $\langle m_{\beta\beta} \rangle < [0.31 - 0.59]$  eV). This limit could be enhanced by using a multivariate analysis, similarly to what is done in other double beta decay experiments, taking advantage of the several topological variables offered by SuperNEMO.

Recent studies have shown that the 25 Gauss magnetic field would be distorted by detector materials, especially the calorimeter magnetic shields. In this context, we studied the influence of this field on the demonstrator sensitivity. Switching-off the field would enhance the expected number of  $2e$  topologies, especially for background processes, and decrease the sensitivity. This effect is compensated by applying optimised topological cut-offs which are useful with such a level of background. Finally, without magnetic field, the SuperNEMO demonstrator would set a limit on the sensitivity of  $T_{1/2}^{0\nu} > 6.1 \times 10^{24}$  years ( $\langle m_{\beta\beta} \rangle < [0.24 - 0.46]$  eV), taking into account the specified activities, a 13% increase on  $T_{1/2}^{0\nu}$  compared with the on-field case. With the measured activities,  $T_{1/2}^{0\nu} > 3.7 \times 10^{24}$  years ( $\langle m_{\beta\beta} \rangle < [0.30 - 0.58]$  eV), an improvement of 3% compared with the on-field case. Simulations with a mapped field have shown that the signal and background selection efficiencies would be degraded by a non-uniform, more realistic magnetic field.

Like its predecessor, the SuperNEMO demonstrator was designed to study several isotopes, such as the  $^{150}\text{Nd}$ . Assuming the target background activities are reached for  $^{150}\text{Nd}$  sources, the SuperNEMO demonstrator would achieve a  $T_{1/2}^{0\nu} > 2.2 \times 10^{24}$  years ( $\langle m_{\beta\beta} \rangle < [0.15 - 0.51]$  eV).

Finally, assuming we reach the target background levels, the SuperNEMO final detector would achieve an unprecedented limit of  $T_{1/2}^{0\nu} > 5.4 \times 10^{25}$  years for  $^{82}\text{Se}$  sources, corresponding to  $\langle m_{\beta\beta} \rangle = [0.079 - 0.15]$  eV. For  $^{150}\text{Nd}$  sources, the half-life  $T_{1/2}^{0\nu} > 2.4 \times 10^{25}$  years would be reached. This corresponds to  $\langle m_{\beta\beta} \rangle = [0.046 - 0.15]$  eV, better than for  $^{82}\text{Se}$  sources, thanks to its higher phase-space factor.

To go further in this study, the SuperNEMO collaboration would study the influence on the sensitivity of external backgrounds, coming from detector materials as well as the laboratory. Also, more realistic performances of the detector, as well as field variations have to be implemented in the software for the simulations to reproduce more accurately the data.

As the  $^{208}\text{Tl}$  background is higher than specified, and topological cut-offs are not strongly efficient to reduce its contribution, the next chapter focuses on setting up a specific technique to reject this internal background.

---

<sup>6</sup>The real mass of isotope is 6.23 kg, then to achieve a 17.5 kg.y exposure, the demonstrator should run a little more than two years and a half.

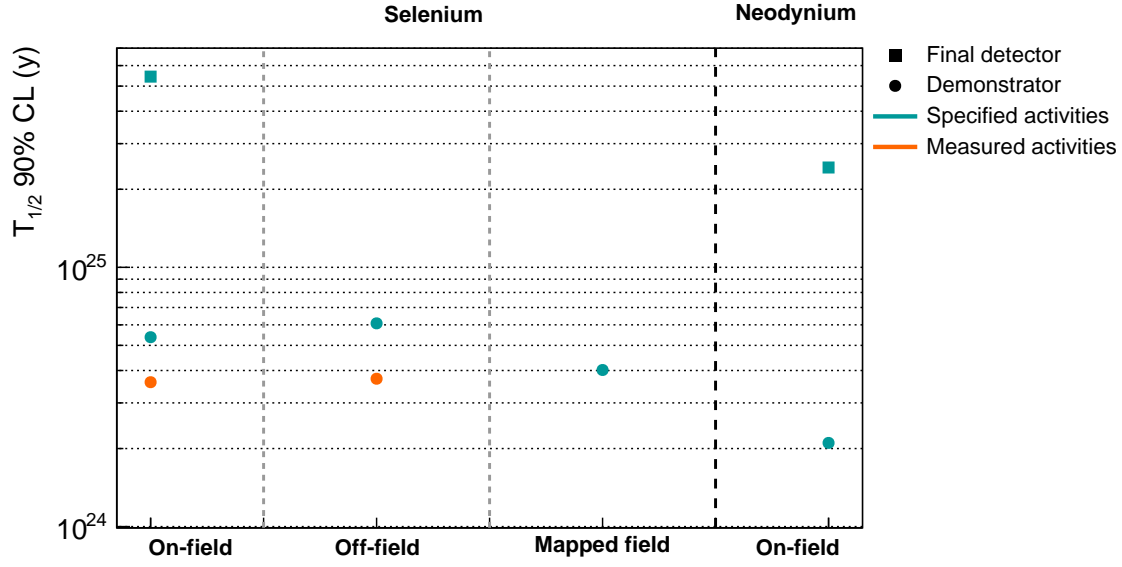
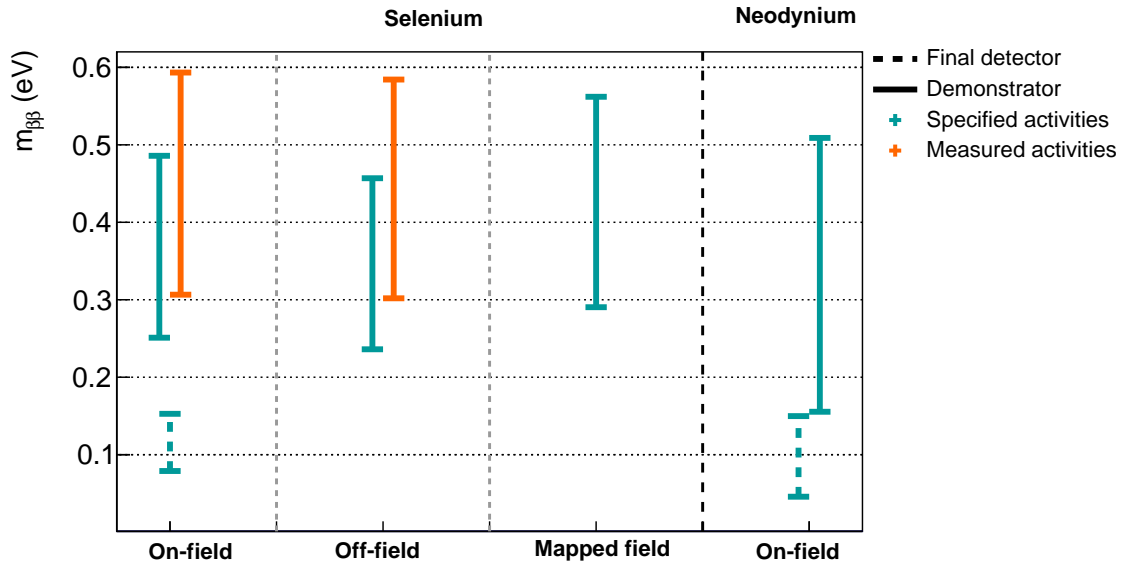
(a)  $T_{1/2}^{0\nu}$  (90% CL) limits.(b)  $m_{\beta\beta}$  limits.

Figure 3.11: Summary of limits set on  $T_{1/2}^{0\nu}$  (a) and  $m_{\beta\beta}$  (b) for each case dealt with in this chapter. First-order and optimised topological cut-offs have been applied. Regions of interest have been optimised for each case.





## Improvement of the internal Thallium-208 background rejection

At the end of September 2018, the 34 enriched-Selenium source foils were installed on the demonstrator. At this time, the internal  $^{208}\text{Tl}$  and  $^{214}\text{Bi}$  activities of these sources had already been measured by the BiPo detector. Also, the Radon concentration in the chamber was extrapolated from Radon emission measurements of the tracker components with a concentration line for an incoming gas flow of  $2 \text{ m}^3/\text{h}$ . We described in the previous chapter the impact of these activities on the final detector sensitivity to the  $0\nu\beta\beta$  decay, and set up optimised topological selections adjusted to reject the Radon background.

However,  $^{208}\text{Tl}$  disintegrations in the sources also remains a troublesome background, even for  $\beta\beta$  emitters with a high  $Q_{\beta\beta}$ . Indeed, it contributes at high energies (up to 4 MeV on the two electrons energy sum spectrum), because of the internal conversion of the 2.615 MeV  $\gamma$ -ray. In a context where the  $^{208}\text{Tl}$  contamination is higher than expected inside the sources, we focus in the current chapter on rejection techniques peculiarly adapted to reject internal  $^{208}\text{Tl}$  events. We study the influence of these additional techniques on  $0\nu\beta\beta$  events selection, and evaluate the impact on final detector sensitivity. Impact of the calorimeter timing performances on these techniques are also addressed in this chapter.

### 4.1 Motivations

In Chapters 2 and 3, we presented the specifications set on the background activities, in order to reach the target limit on the  $0\nu\beta\beta$  process half-life of the  $^{82}\text{Se}$  in 5 years, with 100 kg of isotope. The Tab. 2.3 given in Chapter 2 summarises the target  $^{208}\text{Tl}$ ,  $^{214}\text{Bi}$  and  $^{222}\text{Rn}$  activities, and provides a comparison with those measured by the collaboration. The BiPo detector was capable of giving an upper limit on the  $^{214}\text{Bi}$  level of  $\mathcal{A}^{\text{Bi}} < 290 \text{ } \mu\text{Bq/kg}$  at 90% CL, and future more precise measurements with SuperNEMO demonstrator will constraint this value. The BiPo measurements also showed that the  $^{208}\text{Tl}$  contamination is about 30 times greater than expected on average. We give in Tab. 4.1 the number of expected background events for the measured activities (taking the upper limit for  $^{214}\text{Bi}$

#### 4. IMPROVEMENT OF THE INTERNAL THALLIUM-208 BACKGROUND REJECTION

contamination), for the demonstrator and final detector. With an activity fixed to

Exposure ROI (MeV)	Demonstrator 17.5 kg.y [2.7;3.3]	Detector 500 kg.y [2.6;2.95]
$2\nu\beta\beta$	0.383	104
$^{208}\text{Tl}$	1.09	21.2
$^{214}\text{Bi}$	1.42	110
$^{222}\text{Rn}$	0.0782	6.11

Table 4.1: Expected number of background events in the  $2e$  topology, in optimised energy ranges for the SuperNEMO demonstrator (17.5 kg.y) and the final detector (500 kg.y exposure). The  $2\nu\beta\beta$  half-life is taken as  $T_{1/2}^{2\nu} = 9.39 \times 10^{19}$  y, and the measured background activities are considered (with the upper limit for  $^{214}\text{Bi}$  contamination). The topological selections have been optimised:  $P_{int} > 4\%$  and  $|\Delta Z| < 80$  mm. ROI are optimised to maximise the  $T_{1/2}^{0\nu}$  limit at 90% (see Chapter 3).

the measured one, the  $^{208}\text{Tl}$  background does not affect significantly the sensitivity of the demonstrator (17.5 kg.y exposure) as only one event is expected in the optimised [2.7;3.3] MeV energy region, after first-order and topological cut-offs were applied. On the other hand, this background could be harmful for the final detector (500 kg.y exposure), with 21 events expected in the region of interest [2.6;2.95] MeV. To overcome this effect, it is interesting to set a specific method designed to reject  $^{208}\text{Tl}$  events.

In the next section, we describe the specific features of the Thallium internal background. We develop a new technique of rejection, especially designed to identify internal  $^{208}\text{Tl}$  events, based on several Time-of-flight computations.

## 4.2 The internal $^{208}\text{Tl}$ background

As described in Chapter 2, radioactive isotope disintegrations inside the source foils can occasionally produce two-electron events, and thus can mimic  $\beta\beta$ -decay events. The  $^{208}\text{Tl}$ , a progeny of  $^{232}\text{Th}$ , is one of the largest contribution to the internal background. Two electrons can be produced via a  $\beta$ -decay followed by a Møller scattering,  $\beta$ -decay to an excited state with the subsequent internal conversion, or due to Compton scattering of the de-excitation photon.

The disintegration scheme of  $^{208}\text{Tl}$  isotope is presented in Fig. 4.1. This shows that  $^{208}\text{Tl}$  always  $\beta$ -decays to an excited state of the  $^{208}\text{Pb}$  daughter nuclei. In more than 99 % of the decays, at least 2  $\gamma$ 's are expected after the  $\beta$  emission. For  $0\nu\beta\beta$  detection of isotopes with high  $Q_{\beta\beta}$ , the most dangerous mode of  $\beta\beta$ -like events production comes from the internal conversion of the 2.615 MeV- $\gamma$ , resulting in one electron with an energy of 2.5 MeV approximately and a beta-electron with a continuous spectrum between 0 and  $\sim 1.5$  MeV. Thus  $^{208}\text{Tl}$  events with a total energy greater than 2.7 MeV can populate the region of interest.

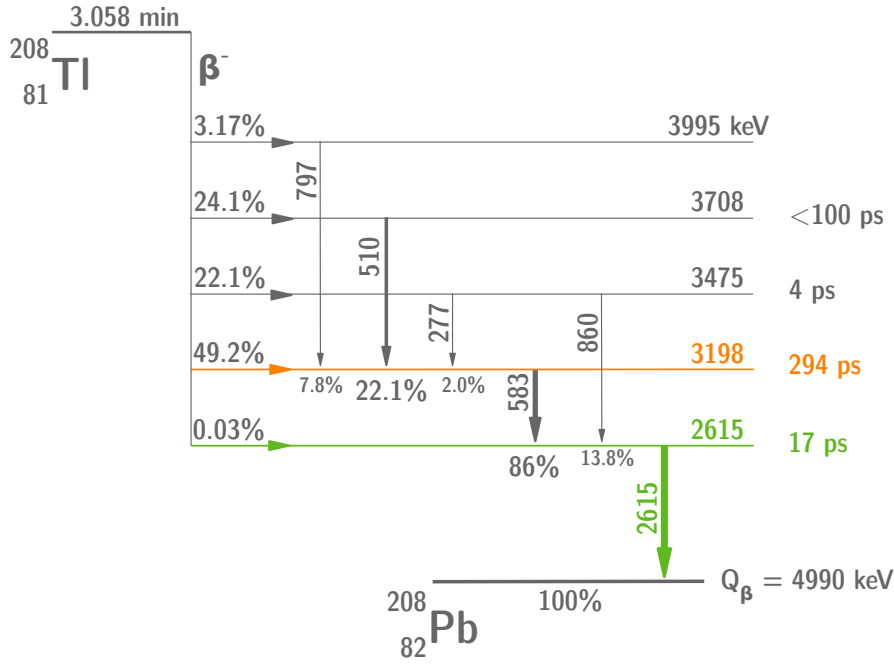


Figure 4.1: A simplified disintegration scheme for the  $^{208}\text{Tl}$  isotope. 81 % of the disintegration pass through the 294 ps metastable energy level (orange). All disintegration go through the 2.615 MeV energy level (green), where an orbital electron is ejected in 0.246 % of the cases through the internal conversion process.

### 4.2.1 The internal conversion process

An excited nucleus will practically constantly achieve a transition to a lower state by one of two processes: the emission of a  $\gamma$ -ray, or the ejection of one of the orbital electrons. The latter, called *internal conversion* (frequently abbreviated IC), is a second-order process, where an electron couples to a proton inside the excited nucleus. Thus, in such a radioactive decay, the de-excitation energy of the nucleus is transferred *directly* to a  $j$ -shell electron ( $j = K, L, M \dots$ ). A high-energy electron is therefore emitted from the atom, and carry off the energy

$$E_{IC} = E_\gamma - E_j \quad (j = K, L, M \dots), \quad (4.1)$$

where  $E_j$  is the binding energy of the electron in the  $j$ -shell, and  $E_\gamma$  is the energy of the  $\gamma$ -ray.

This mechanism is possible because there is a non-zero probability of finding the electron within the nucleus, that is to say, the wave-function of the electron can penetrate the volume of the nucleus. Consequently, due to their high nuclear penetration, electrons coming from the  $1s$  state are more likely to be ejected (this transition is called  $K$  internal conversion). Although electrons coming from  $2s$ ,  $3s$  and  $4s$  states ( $L$ ,  $M$  or  $N$  internal conversions) have also a non-zero probability to undergo this process. After the electron ejection, the hole in the corresponding shell is filled by an electron from a higher energy level, emitting characteristic  $X$ -rays, Auger electrons, or both.

For a given transition, the internal conversion coefficient of the electron in the  $j$ -shell, is defined by

$$\alpha_j = \frac{P_{IC,j}}{P_\gamma}, \quad (4.2)$$

where  $P_{IC,j}$  is the  $j$  conversion electron emission probability, and  $P_\gamma$  is the  $\gamma$ -ray emission probability. The total coefficient is

$$\alpha_T = \sum_{j=K,L,M\dots} \alpha_j. \quad (4.3)$$

These coefficients are given in Tab. 4.2 for the 2.615 MeV energy level of  $^{208}\text{Tl}$  isotope. Therefore, in 0.246 % of the cases, the  $^{208}\text{Pb}$  excited nucleus will

$j$ -shell	$K$	$L$	$M$	Total
IC coefficients (%)	0.1708	0.0292	0.00685	0.246

Table 4.2: Internal conversion coefficients for the 2.615 MeV  $\gamma$ -ray of the  $^{208}\text{Tl}$  decay scheme.

undergone an internal conversion corresponding to the 2.615 MeV energy level.

#### 4.2.2 $^{208}\text{Tl}$ disintegrations in the $2e$ channel

Finally, a  $^{208}\text{Tl}$  decay can present a two-electrons topology when, after the  $\beta$  emission, an electron is ejected from the atom through internal conversion. Especially, when this energy transfer corresponds to the 2.615 MeV  $\gamma$ -ray, the ejected electron carry off a significant energy, depending on its initial binding energy with the nucleus. For instance an orbital electron from the  $K$ -shell is ejected with an energy  $E_{IC,K} = 2.526$  MeV ( $\alpha_K = 0.17\%$ ). This decay is therefore likely to contribute in the region of interest for the  $0\nu\beta\beta$  search of  $^{82}\text{Se}$ , or even  $^{150}\text{Nd}$ .

In the  $2e$  channel, optimised topological cut-offs, based on time-of-flight computation and the distance between vertices, were presented in the previous chapter. They are mostly efficient in rejecting the non-internal  $^{222}\text{Rn}$  events. After a brief presentation of the simulations carried out as part of this analysis, we remind and specify the internal probability computation, and present a new selection, also based on the time-of-flight computation, to reject the  $^{208}\text{Tl}$  background.

### 4.3 Simulated demonstrator performances

The background model used in the framework of this study has already been described in detail in the previous chapter. Nevertheless, calorimeter performances implemented in the Falaise software have been modified in this study. Indeed, one of the main goal is to evaluate the influence of the calorimeter timing performances on the  $^{208}\text{Tl}$  background rejection. This study was led before the commissioning phase of the calorimeter when timing performances were characterised only for few optical modules, and before their installation at Modane [15]. An encouraging

value for the uncertainty on the calorimeter time measurement of 248.3 ps for incoming electrons and 341.8 ps for photons were provided for the best optical module tested (Fig. 4.2). In this context, before the full calorimeter calibration

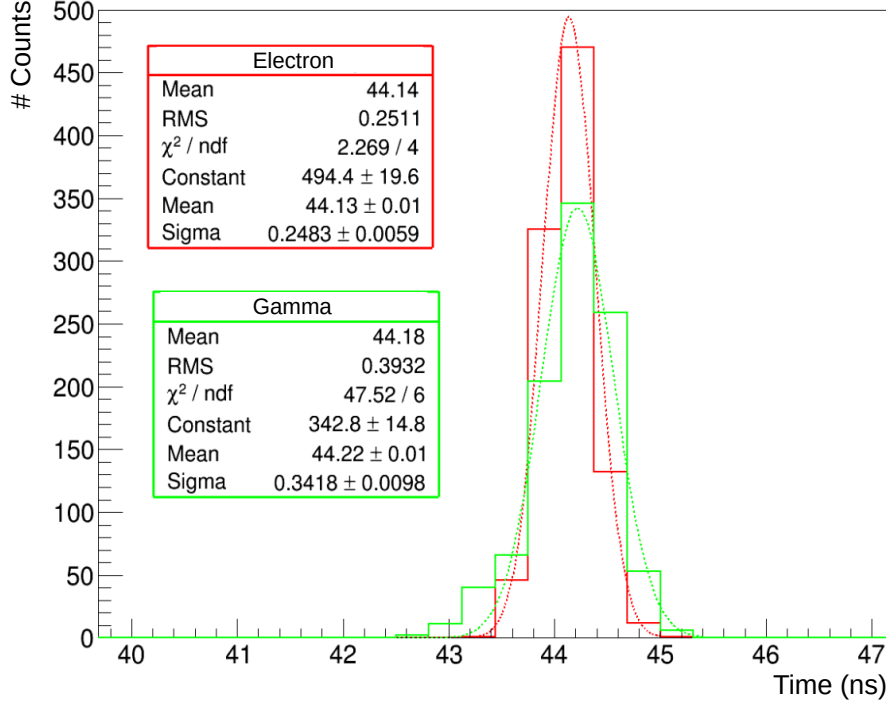


Figure 4.2: Time distribution of the trigger time of an optical module in the case of electrons (red) and gamma radiation (green) depositing an energy of 1 MeV in the scintillator. The trigger threshold is set at 45 mV and corresponds to an energy of 0.150 MeV. Adapted from [15].

in Modane, we would give an overview of the influence of these performances on the  $^{208}\text{Tl}$  background rejection. To do so, signal and background simulations were performed supposing the optical modules measure perfectly the particle time-of-flights, by setting to zero the time uncertainty at the level of the calibration module in the Falaise pipeline. I wrote a Root code allowing to degrade the precision on time measurements for it to be set by the user to the desired accuracy.

All of the simulations produced for this analysis were generated using the official Falaise pipeline, and are made available to the collaboration in the common SuperNEMO repository at the IN2P3 computing centre platform. The same code described in the previous chapter has been used for this study, including the Particle Identification module, the module I wrote and the Root code pipeline. An additional set of codes have been developed in order to degrade the simulated calorimeter resolution as well as to compute the analysis tools described in the following.

In the first instance we set the reasonable value of 200 ps for the measurement uncertainty. In Sec. 4.5.4 the influence of this parameter on the  $^{208}\text{Tl}$  rejection is provided, and we give final sensitivity results according to it in Sec. 4.6.

## 4.4 Rejection of $^{208}\text{Tl}$ with a time-of-flight criterion

The internal probability, based on time-of-flight computation, quantifies the likelihood that two particles were emitted inside the source foils, from the same vertex. Unless it is a useful tool, we would implement a new one, also based on time-of-flight, taking into account the possible delay between the two incoming electrons due to the  $^{208}\text{Pb}$  metastable state.

### 4.4.1 The internal probability

As part of the analysis pipeline, this tool is widely employed in NEMO-3 and SuperNEMO, for background rejection purposes. We present it in detail in Chapter 2 and examine an example of its usefulness in Chapter 3. Nevertheless, in the framework of this analysis we need to perform our own calculation of internal probability, after the reconstruction pipeline, because the simulations are performed for an ideal value of the optical module performances. That is an opportunity to come back to this tool and to clarify certain points.

The calculation of the internal  $\chi^2$  is reminded in Eq. (4.4), for two detected electrons, as a function of the expected time-of-flights,  $t^{\text{exp}}$ , the experimentally measured time-of-flights,  $t^{\text{meas}}$ , as well as the total uncertainty on the time-of-flight measurement:

$$\chi_{int}^2 = \frac{((t_1^{\text{meas}} - t_1^{\text{exp}}) - (t_2^{\text{meas}} - t_2^{\text{exp}}))^2}{\sigma_{t_1}^2 + \sigma_{t_2}^2 + \sigma_{\beta_2}^2 + \sigma_{\beta_1}^2 + \sigma_{l_1}^2 + \sigma_{l_2}^2}. \quad (4.4)$$

$\sigma_{t_i}$  is the uncertainty on the measured time-of-flight.  $\sigma_{\beta_i}$  and  $\sigma_{l_i}$  are the uncertainties on the expected time-of-flight brought by the uncertainty on particle energies and track lengths, respectively. The denominator square root corresponds to the total uncertainty, whose measured time-of-flight uncertainty is simulated as zero and degraded afterwards.

In the official SuperNEMO reconstruction pipeline,  $\sigma_l = \sigma_{l_1} = \sigma_{l_2} = 70$  ps for electron particles. As we simulated perfect calorimeters, we check that this parameter is correctly evaluated in order to implement it in our own off-line Root code pipeline.

### Optimisation of $\sigma_l$

One way to examine if  $\sigma_l$  is well-evaluated is to look at the flatness of the internal probability distribution for  $0\nu\beta\beta$  events in the  $2e$  topology, for which a flat distribution is expected. Indeed, the slope of this distribution provides pertinent information to check the estimation of uncertainties. The flatter the distribution, the more correctly uncertainties are estimated.

Therefore, for this optimisation, we use  $2e$  topologies of signal simulations inside the source foils. Discrete values of  $\sigma_l$  running from 0.01 to 0.1 ns are used to compute the internal probability distributions of these events. For each distribution, a linear fit is performed on the reduced range  $P_{int} \in [0.1; 1]$  in order to

avoid the peak at low internal probabilities. The *flatness parameter*  $a_F$  is defined as the slope parameter of the linear fit. The optimisation then consists in finding the value of  $\sigma_l$  for which the parameter  $a_F$  is cancelled, which corresponds to the best estimate for  $\sigma_l$ .

In Fig. 4.3 is given the slope  $a_F$  as a function of  $\sigma_l$ . For  $\sigma_l = 70$  ps,  $a_F > 0$ ,

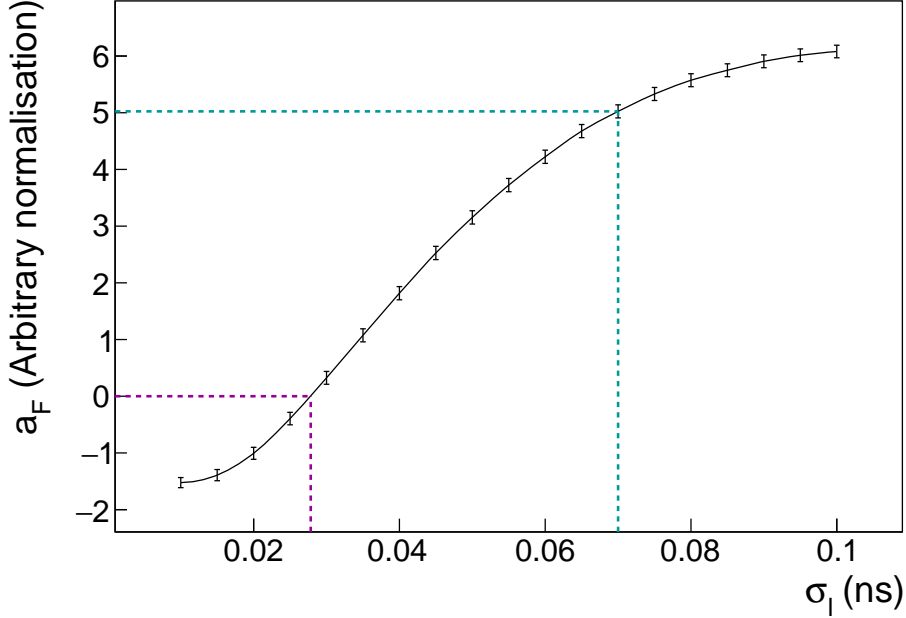


Figure 4.3: Slope  $a_F$  as a function of the time uncertainty due to the reconstructed track length  $\sigma_l$ . The former value used in the SuperNEMO reconstruction pipeline is pointed out by blue dashed lines. The value kept for  $\sigma_l$  is the one for which  $a_F = 0$ ,  $\sigma_l = 27.8 \pm 0.8$  ps, showed by purple dashed lines.  $P_{int}$  is calculated for  $0\nu\beta\beta$  decays simulated inside the source foil, with first order cut-offs applied.

revealing an overestimation of uncertainties in the computation of the internal  $\chi^2$  in the SuperNEMO reconstruction pipeline, at the Particle Identification module level. The optimised value, kept for the further analysis, is  $\sigma_l = 27.8 \pm 0.8$  ps. In Fig. 4.4 is displayed the internal probability distributions for these two values of the  $\sigma_l$  parameter,  $\sigma_l = 70$  ps and  $\sigma_l = 27.8$  ps.

Let us notice that normally  $\sigma_l$  should depend on the track length as well as the energy, especially as multiple scatterings in the tracker have a more notable impact for low energy electrons. A more complete analysis would then compare the simulated track lengths with the reconstructed ones, for different energy simulated sets of mono-kinetic electrons, to evaluate this dependence. Nevertheless, our optimisation is good enough for the current analysis. Discussions are in progress to modify this parameter in the SuperNEMO software.

The internal probability is principally designed to reject non-simultaneous events coming from the source foils. Therefore, it is extremely effective in rejecting  $^{222}\text{Rn}$  events produced far from the source foils. Even if it is less, this criterion is also effective in rejecting  $^{208}\text{Tl}$  events, due to the existence of a metastable state

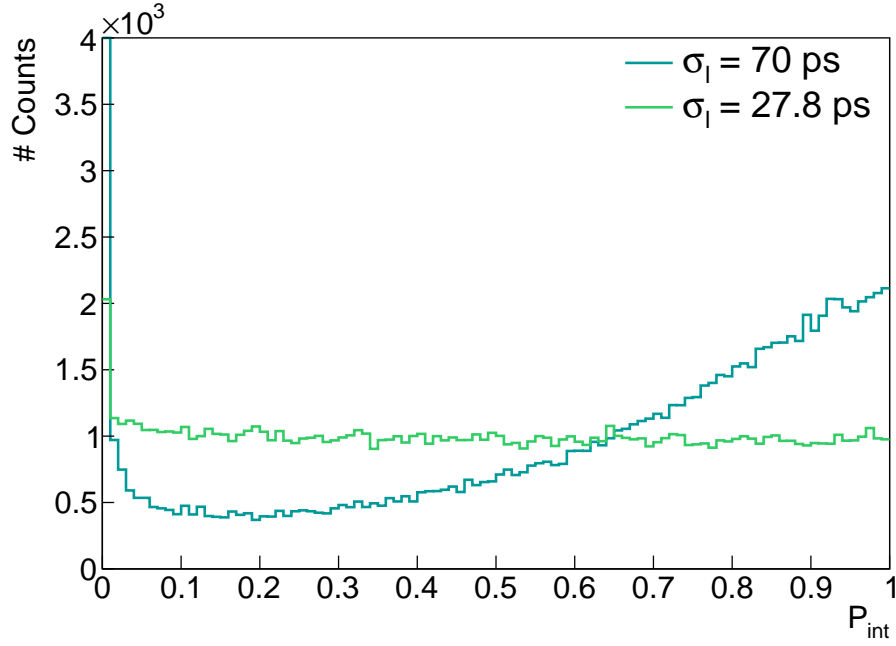


Figure 4.4: Internal probability distributions for  $\sigma_l = 70$  ps (blue) and  $\sigma_l = 27.8$  ps (green).  $P_{int}$  is calculated for  $0\nu\beta\beta$  decays simulated inside the source foil, with first order cut-offs applied.

for the daughter nucleus of  $^{208}\text{Tl}$ . Therefore the emission of the 2.615 MeV- $\gamma$  is in most of the cases delayed. But to describe even better these internal conversion events we would set up a new probability law expressing the hypothesis that a given event is from a  $\beta$ +IC delayed  $^{208}\text{Tl}$  disintegration.

#### 4.4.2 The exponential probability for $^{208}\text{Tl}$ events

According to the disintegration scheme of the  $^{208}\text{Tl}$  isotope (Fig. 4.1), there is an 81 % probability of passing through the 294 ps metastable level. After that, to reach the ground state of  $^{208}\text{Pb}$ , the excited nucleus has 100% of probability to decay through the 2.615 MeV energy level. At this occasion, in 0.246% of cases (Tab. 4.2), one of the orbital electrons is ejected from the atom following the internal conversion process. To summarise, for 0.20 % of the total  $^{208}\text{Tl}$  decays, a  $\beta$  particle is emitted, and a delayed orbital electron is ejected through internal conversion of the 2.6 MeV- $\gamma$ . Furthermore,  $X\%$  of the events with an energy sum greater than 2.7 MeV (the ROI low bound) are from delayed internal conversion decays and could be harmful for the  $0\nu\beta\beta$  search. We aim to use this delayed electron to discriminate  $^{208}\text{Tl}$  internal background from the  $0\nu\beta\beta$  signal.

##### 4.4.2.1 Probability density function

For a given detected  $2e$  topology, we define the  $\Delta t^{meas}$  parameter as

$$\Delta t^{meas} = t_1^{meas} - t_2^{meas}, \quad (4.5)$$



where  $t_1^{meas}$  and  $t_2^{meas}$  are the two measured time-of-flights, where  $t_2$  stands for the electron of lowest energy, and  $t_1$  for the one of highest energy. If this  $2e$  topology corresponds to a delayed  $^{208}\text{Tl}$  event, then the electron of lowest energy is supposed to be a  $\beta$  particle and the one of highest energy an electron coming from an internal conversion, delayed in average of 294 ps. Assuming an ideal calorimeter perfectly measuring time-of-flights and energies, the  $\Delta t$  distribution for such delayed events would be a decreasing exponential, with the decay parameter  $\tau = 294$  ps. However, in actual conditions, this exponential is degraded by the uncertainties on time-of-flight measurements detailed in Eq. (4.4). These are embedded by a Gaussian distribution centred around  $\mu = 0$  ps with a given width  $\sigma$ . Therefore, to each  $2e$  topology is associated a probability density function which is the convolution between an exponential and a Gaussian distribution, written down as  $(E \otimes G)_{\tau,\mu,\sigma}(\Delta t)$ . The corresponding value of  $\Delta t^{meas}$  is then found somewhere on this distribution, and will serve us to define the so-called *exponential probability*,  $P_{exp}(\Delta t^{meas})$ , which is the probability that this event comes from a  $\beta$ +IC delayed decay.

#### 4.4.2.2 Exponential probability

We wish to define this probability following the same principle as for the internal probability, for comparison purposes. Therefore, we would obtain the maximal value  $P_{exp} = 1$  when the value of  $\Delta t$  is the most probable, i.e. when  $\Delta t$  is of the order of the mean of the  $(E \otimes G)_{\tau,\mu,\sigma}(\Delta t)$  distribution. On the other hand, minimal values for  $P_{exp}$  would be reached for less probable values of  $\Delta t$ , so  $P_{exp} \xrightarrow{|\Delta t| \rightarrow +\infty} 0$ .

To do so, the  $(E \otimes G)_{\tau,\mu,\sigma}(\Delta t)$  distribution is normalised and the exponential probability is defined as

$$P_{exp}(\Delta t^{meas}) = \int_{-\infty}^{\Delta t^{meas}} (E \otimes G)_{\tau,\mu,\sigma}(t) dt + \int_{\Delta t_{sym}^{meas}}^{-\infty} (E \otimes G)_{\tau,\mu,\sigma}(t) dt, \quad (4.6)$$

where  $\Delta t_{sym}^{meas}$  is defined such that  $(E \otimes G)_{\tau,\mu,\sigma}(\Delta t_{sym}^{meas}) = (E \otimes G)_{\tau,\mu,\sigma}(\Delta t^{meas})$ . A graphical representation is given in Fig. 4.5. In this example the distribution corresponds to  $(E \otimes G)_{\tau,\mu,\sigma}(\Delta t)$  with  $\tau = 294$  ps and  $\mu = 0$  ps and the total time uncertainty is calculated taking  $\sigma_l = 27.8$  ps and  $\sigma_t = 200$  ps for 1 MeV electrons. The two integrals whose sum is given in the Eq. (4.6) are represented by two red-coloured areas. As explained, each probability density function is defined for a single 2-electrons event, because the time-of-flight uncertainty depends on the electron measured energy and on the track length. In the given example, we considered two particles interacting inside the calorimeter with an energy of 1 MeV each.

In fig. 4.6 are presented exponential probability distributions for  $2e$  topologies selected of  $^{208}\text{Tl}$  and  $0\nu\beta\beta$  simulations inside the source foils. As expected, the distribution is flat, since this probability was defined in the same way as the internal probability.

Now analysis tools are defined, the following sections focus on the event selections using them, the way to optimise them and their influence on the final detector sensitivity.

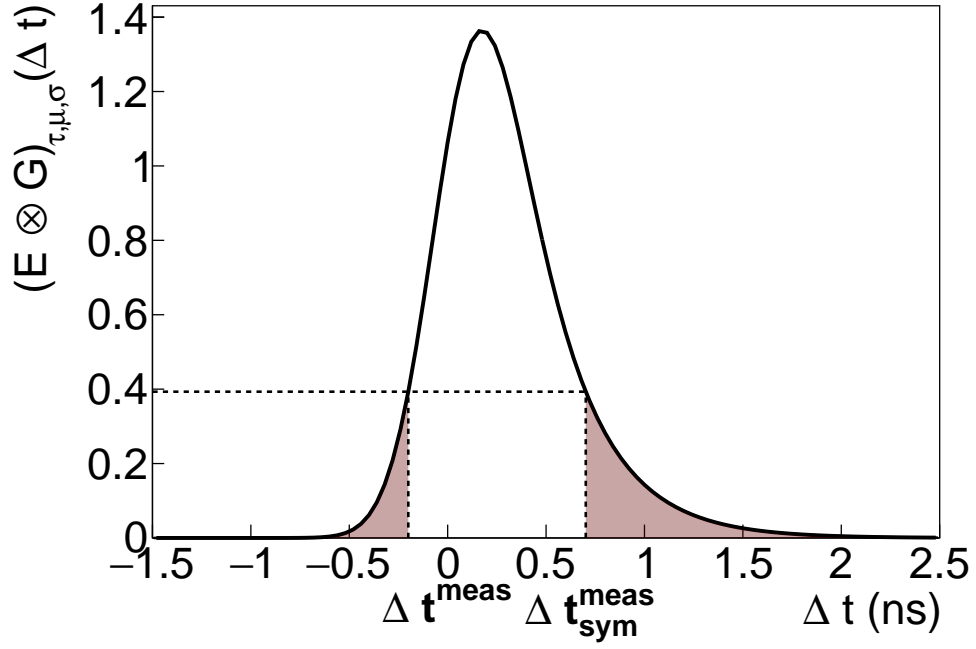


Figure 4.5: Normalised convolution distribution  $(E \otimes G)_{\tau, \mu, \sigma}(\Delta t)$ . The parameters are  $\tau = 294$  ps,  $\mu = 0$  ps and  $\sigma = \sigma_{tot}$ , computed with  $\sigma_l = 27.8$  ps and  $\sigma_t = 200$  ps.

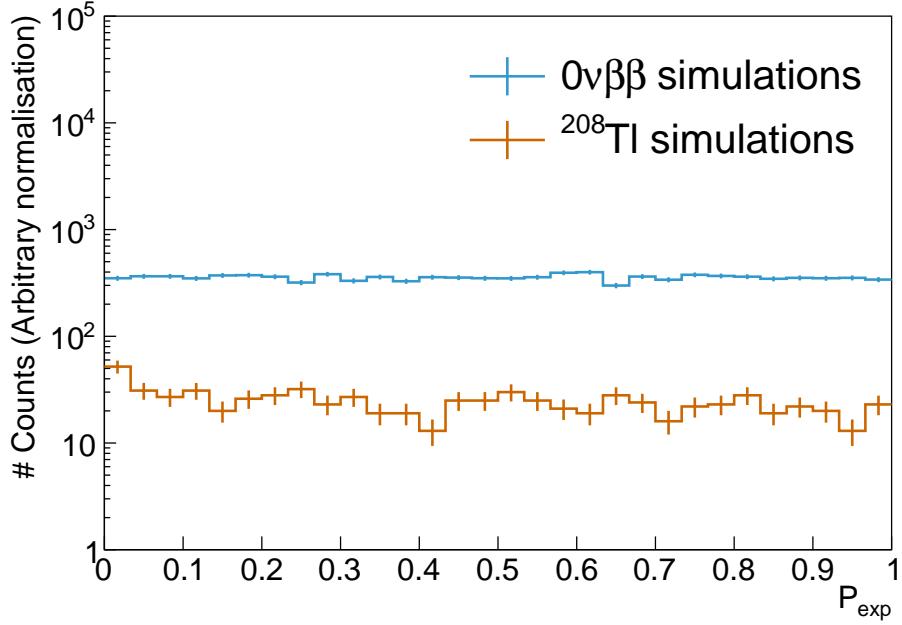


Figure 4.6: Exponential probability distribution for  $^{208}\text{Tl}$  (orange) and  $0\nu\beta\beta$  simulations (blue), for  $2e$  topologies with an electron energy sum greater than 2.7 MeV (discussed in Sec. 4.5).  $\sigma_t = 200$  ps,  $\sigma_l = 27.8$  ps.

## 4.5 Event selection

Now the exponential probability tool has been defined, the aim of this analysis is to set up events selections focusing on delayed  $^{208}\text{Tl}$  events rejection. Basic cut-offs are described, and compared with a more elaborated selection using these two probabilities. The influence of the uncertainty  $\sigma_t$  on time measurement is discussed at the end of the section.

### 4.5.1 Energy selection

Based on the conclusions given in the previous chapter, the lower bound of the region of interest optimising the search of  $0\nu\beta\beta$  decay stands at the electron energy sum of 2.7 MeV for the demonstrator. From this energy,  $2e$  topologies for  $^{208}\text{Tl}$  are mainly populated by  $\beta$  decays followed by the internal conversion of the 2.615 MeV  $\gamma$ -ray. In the following, we therefore focus only on events with a sum in energy of the two detected electrons greater than 2.7 MeV.

### 4.5.2 Time-of-flight cut-off

Before using the two internal and exponential probabilities, a simple cut-off using the electron time-of-flight is explored. Indeed, we are especially focused on rejecting the internal  $^{208}\text{Tl}$  events for which the successive  $\beta$  and  $\gamma$ -rays emissions went through the 294 ps metastable state. For these decays, we are expecting the particle of highest energy to be delayed compared with the one of lowest energy. Each term in Eq. 4.5 corresponds to what it took for a particle to travel from the source to the calorimeter and depends on the time it spent in the source after emission, as well as how long it took to cross the tracker. In order to remove from  $\Delta t^{meas}$  the dependency on travel time in the tracker, we define the corrected time difference as

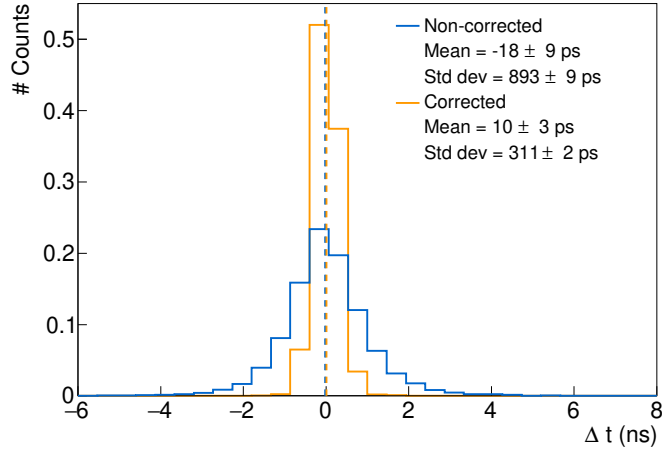
$$\Delta t^{corr} = t_1^{corr} - t_2^{corr} \quad (4.7)$$

$$= (t_1^{meas} - t_1^{exp}) - (t_2^{meas} - t_2^{exp}), \quad (4.8)$$

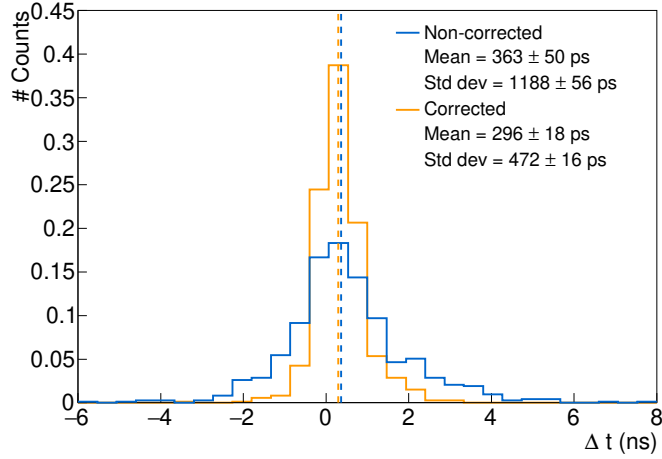
where  $t_i^{corr}$  are the corrected time-of-flights and  $t_i^{exp}$  the expected ones calculated with the particle energy and track length (Eq. 2.2).

The two distributions  $\Delta t^{meas}$  and  $\Delta t^{corr}$  are presented in Fig. 4.7, for  $0\nu\beta\beta$  and  $^{208}\text{Tl}$  simulations inside the source foils. For  $0\nu\beta\beta$  simulations, the  $\Delta t^{corr}$  distribution is centred around zero, as the two electrons are emitted simultaneously inside the source. Then, the correction on time difference only lowers the standard deviation of the distribution. For  $^{208}\text{Tl}$  simulations, the mean of the distribution is slightly shifted towards positive values. Once corrected by the expected times, the mean difference between the two electrons time-of-flights stands at  $296 \pm 18$  ps. This is a direct consequence of the existence of  $\beta$ +IC delayed events, for which the particle of highest energy is expected to hit a calorimeter block at a time  $t_1^{corr} > t_2^{corr}$ . The set up calorimeter time uncertainty at 200 ps allows to be sensitive to this decay as the mean of the distribution is near 294 ps. Therefore,

#### 4. IMPROVEMENT OF THE INTERNAL THALLIUM-208 BACKGROUND REJECTION



(a)  $0\nu\beta\beta$  simulations.



(b)  $^{208}\text{Tl}$  simulations.

Figure 4.7: Corrected (orange) and non-corrected (blue) time-of-flight difference between the two electrons. (a)  $0\nu\beta\beta$  simulations inside the source foils. (b)  $^{208}\text{Tl}$  simulations inside the source foils. The first-order selections have been applied. The two distributions are normalised.  $\sigma_t = 200$  ps and  $\sigma_l = 27.8$  ps.

a simple way of rejecting the  $^{208}\text{Tl}$  delayed events is to consider the sign of  $\Delta t^{\text{corr}}$  and to reject events for which  $\Delta t^{\text{corr}} > 0$ .

By applying this selection on  $2e$  topologies of  $0\nu\beta\beta$  and  $^{208}\text{Tl}$  simulations for which  $E > 2.7$  MeV, we are able to reject 76 % of  $^{208}\text{Tl}$  while selecting 49 % of the  $0\nu\beta\beta$  ( $\sigma_t = 200$  ps). The 49% of selected signal events is expected as the corresponding  $\Delta t^{\text{corr}}$  distribution is symmetrical, unlike the one for  $^{208}\text{Tl}$  events. Although we manage to reject a significant fraction of Thallium events, the impact of this cut is too high on  $0\nu\beta\beta$  events. Moreover, the uncertainties on time-of-flights are not taken into account in the rejection criterion. Later in this chapter we consider different levels for this selection and optimise them according to the  $\sigma_t$  value set up.

### 4.5.3 Probability cut-off

At this level it is interesting to consider the internal and exponential probabilities to describe  $2e$  topologies and attempt to obtain a higher background rejection. They seem to be better tools notably because, unlike the  $\Delta t^{\text{corr}}$  rejection criterion, they do take into account the time-of-flight uncertainties. The first one was already used in Chapter 3, and is a widely-used tool to reject non-internal events. The second was designed specifically for this analysis to identify delayed  $^{208}\text{Tl}$  events, and also depends on the time of flight resolution through the convolution with a Gaussian function.

The idea in this section is to reject  $^{208}\text{Tl}$  events taking into account their two values of internal and exponential probabilities. Then it is interesting to represent them with a two-dimensional binned histogram of  $P_{\text{exp}}$  as a function of  $P_{\text{int}}$ , as done in Fig. 4.8. In this particular example, we picture the variations of  $P_{\text{int}}$  and

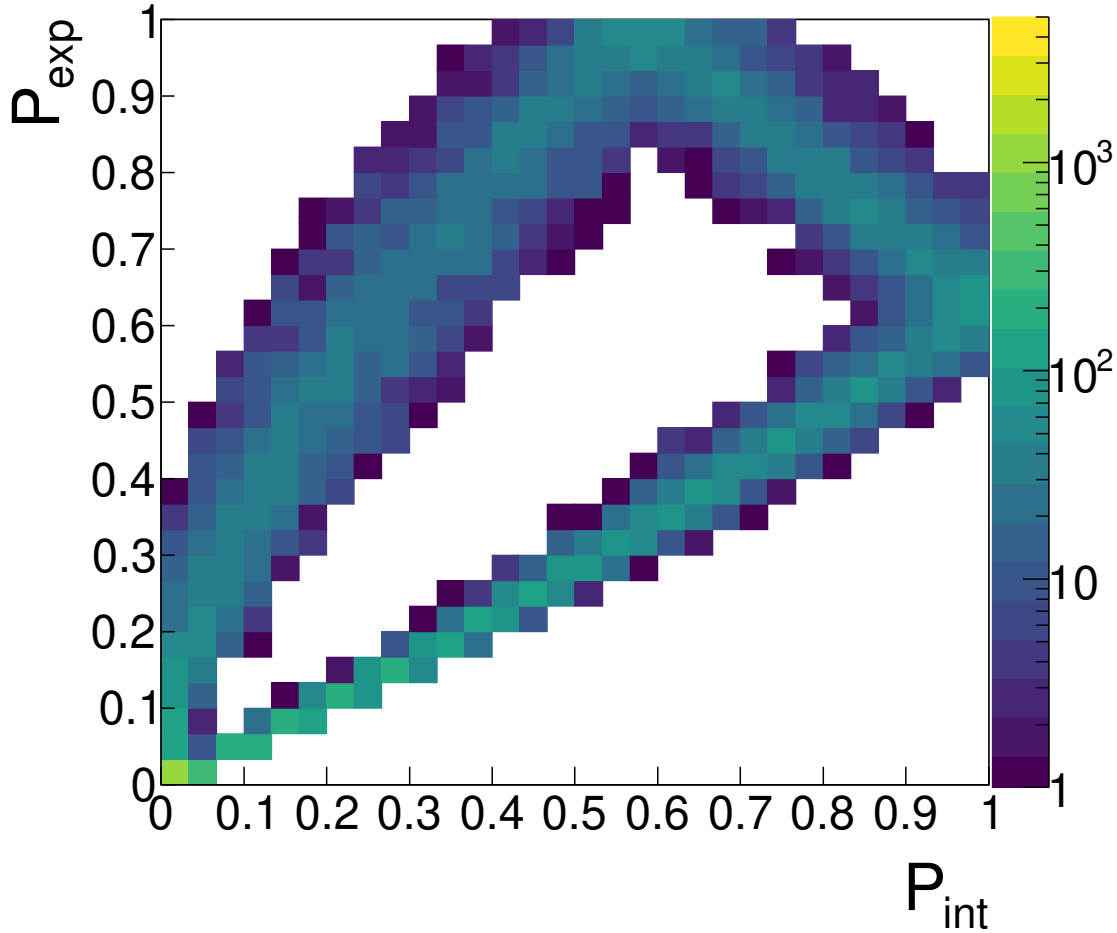


Figure 4.8: Two-dimensional histogram showing the  $P_{\text{exp}}$  variations as a function of  $P_{\text{int}}$  for  $^{208}\text{Tl}$   $2e$  topologies.  $\sigma_t = 200$  ps and  $\sigma_l = 27.8$  ps.

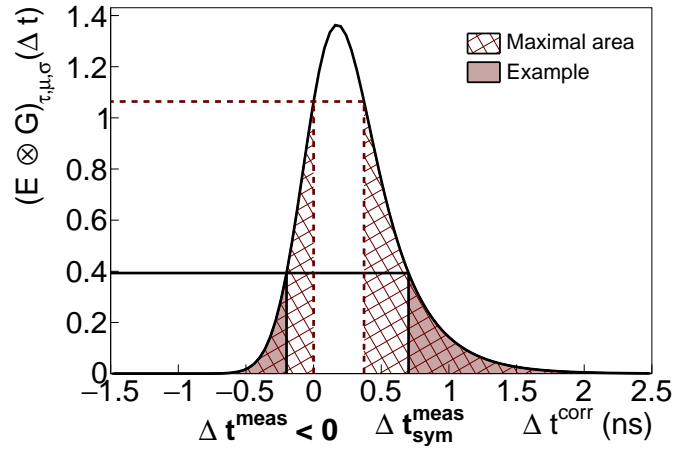
$P_{\text{exp}}$  applying  $\sigma_t = 200$  ps. We clearly distinguish three event populations in this histogram. In order to better understand these variations, we give in Fig. 4.9

three examples of  $(E \otimes G)_{\tau,\mu,\sigma}(\Delta t)$  distributions, each of them illustrating one of the three zones.

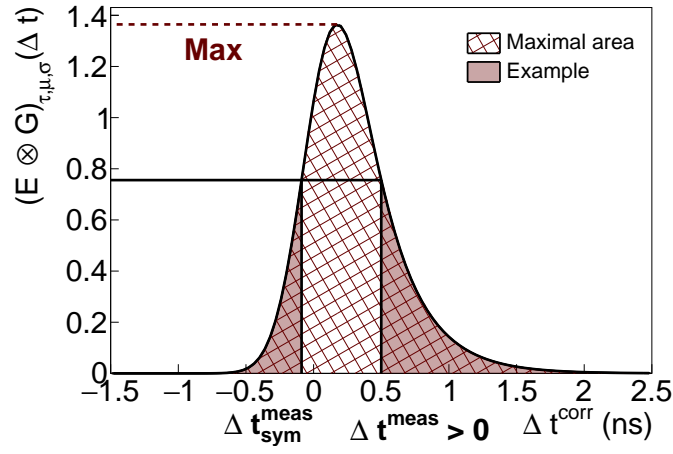
1.  $P_{int} \in [0; 1]$  and  $P_{exp} \in [0; 0.65]$ , with  $P_{int} > P_{exp}$  (Fig. 4.9a):  
This region corresponds to events for which  $\Delta t^{corr} < 0$ . As the internal  $\chi_{int}^2$  distribution is symmetrical, such events can have a value of  $P_{int}$  varying from 0 to 1. Small values of  $P_{int}$  correspond to events with a large negative  $\Delta t^{corr}$  value. Conversely, the exponential distribution is not centred in zero. Therefore, if we limit to events for which the time difference is negative, we reach an upper bound for the value of the integral (0.65 in that case). This bound directly depends on the variations of the exponential distribution, therefore on the  $\sigma_t$  value applied.
2.  $P_{int} \in [0; 0.65]$  and  $P_{exp} \in [0; 1]$ , with  $P_{exp} > P_{int}$  (Fig. 4.9b):  
These events have positive values for  $\Delta t^{corr}$ , beyond the  $(E \otimes G)_{\tau,\mu,\sigma}(\Delta t)$  distribution maximum. The smaller the value of  $P_{int}$ , the lower the probability that both particles were emitted at the same time into the source. Besides, for values of  $\Delta t^{corr}$  highly positives, the value of the exponential probability can reach high values, up to 1. The larger the value of  $\Delta t^{corr}$  in positives, the smaller the value of  $P_{exp}$ .
3.  $P_{int} \in [0.65; 1]$  and  $P_{exp} \in [0.65; 1]$  (Fig. 4.9c):  
This region is also populated by events for which  $\Delta t^{corr} > 0$ . Unlike the previous case, these events have small  $\Delta t^{corr}$  values, meaning below the maximum of the exponential distribution. Also, these events have high internal probability values, as the probability that these two particles were emitted simultaneously is high. In the same way as the first bullet, the value of  $P_{exp}$  is bounded: the lower bound corresponds to the value of the integral when  $\Delta t^{corr} = 0$  (here 0.65). Once again, this bound is deeply related to the value considered for  $\sigma_t$ . The exponential probability can be equal to 1 when  $\Delta t^{corr}$  reaches the maximum of the exponential distribution.

As discussed, the exponential probability quantifies the likelihood that two particles were emitted with a delay corresponding to the radioactive exponential decay with  $\tau = 294$  ps, taking into account the time of flight resolution. Therefore, we are interested in rejecting events for which values of  $P_{exp}$  are high compared with the  $P_{int}$  values. In that case, a simple selection allowing to discriminate signal  $0\nu\beta\beta$  from delayed  $^{208}\text{Tl}$  event consists in rejecting  $2e$  topologies for which  $P_{exp} > P_{int}$  (this cut-off is pictured in Fig. 4.8 by a plain black line). With the previous explanation, we understand that such a cut is strongly linked to the cut on  $\Delta t^{corr}$  presented in the previous sub-section.

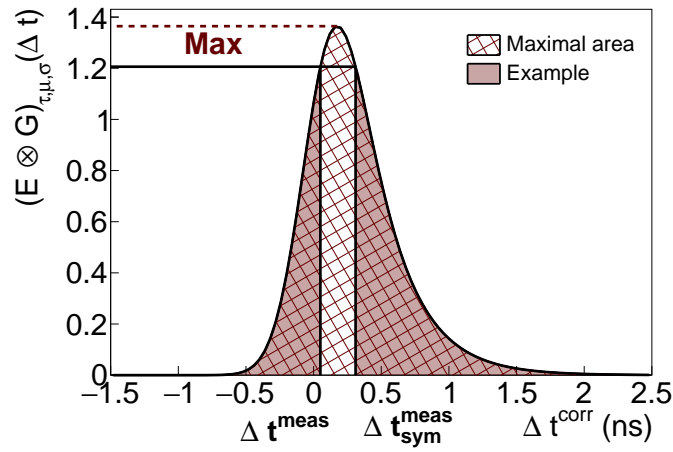
We would like to refine the selection made on the events using the two probabilities. Regarding the biplot presented in Fig. 4.8, the goal is to reject events located in the area 3 and a part of the events located in area 2. Therefore, a more adapted cut-off is to reject events for which  $P_{exp} > 0.65$ . For this selection and  $\sigma_t = 200$  ps, we reject 20% of  $^{208}\text{Tl}$  and keep 84% of  $0\nu\beta\beta$  events. The proportion of signal events kept with this selection is satisfying. Nevertheless the efficiency of



(a)



(b)



(c)

Figure 4.9:  $(E \otimes G)_{\tau, \mu, \sigma}(\Delta t)$  distributions describing the three areas observed in Fig. 4.8. (a)  $\Delta t^{\text{corr}} \in ]-\infty; 0]$ . (b)  $\Delta t^{\text{corr}} \in ]\Delta t_{\text{max}}; +\infty]$ . (c)  $\Delta t^{\text{corr}} \in ]0; \Delta t_{\text{max}}]$ .

$^{208}\text{Tl}$  rejection is almost 4 times lower than for the time-of-flight selection presented in Sec. 4.5.2.

#### 4.5.4 Influence of the calorimeter time resolution

We study in this subsection the influence of the calorimeter timing resolution on event selections, using the cut-offs presented above. We consider values for  $\sigma_t$  in the  $[0 - 400]$  ps range.

In Sec. 4.5.2 we presented rejection efficiencies for a  $\Delta t^{corr} > 0$  ps selection, with  $\sigma_t = 200$  ps. In Fig. 4.10 is presented the  $0\nu\beta\beta$  selection efficiency with the rejection efficiency of  $^{208}\text{Tl}$ , for values of  $\sigma_t$  running from the ideal 0 ps, to 400 ps. Each point corresponds to a  $\Delta t^{corr}$  level applied on the selected  $2e$  topologies, from

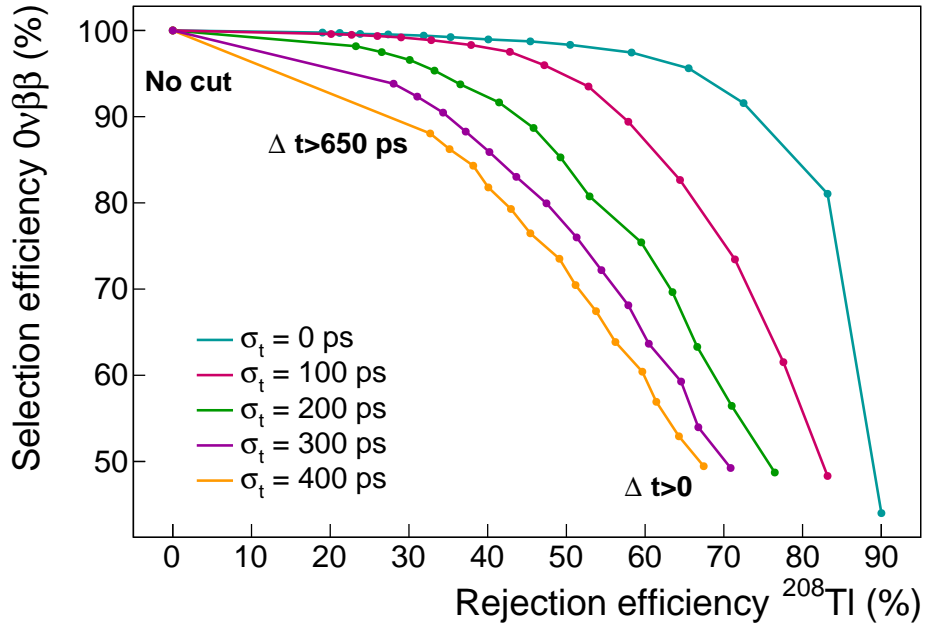


Figure 4.10:  $0\nu\beta\beta$  selection efficiency as a function of  $^{208}\text{Tl}$  rejection. Each curve corresponds to a given value of  $\sigma_t$  from 0 to 400 ps. Each data point corresponds to a minimum value for  $\Delta t^{corr}$  applied on selected 2 topologies from 0 to 650 ps. the optimised value of  $\sigma_t = 27.8$  ps is applied.

$\Delta t^{corr} > 0$  to  $\Delta t^{corr} > 650$  ps. For  $\Delta t^{corr} > 0$  and  $\sigma_t = 200$  ps, we get back to the result given previously. Nevertheless, for this time uncertainty, an optimised value for the  $\Delta t^{corr}$  cut level, called *maximum efficiency point*, is found at  $\Delta t^{corr} > 250$  ps as it optimises the signal selection and  $^{208}\text{Tl}$  background rejection efficiencies. Such a point can be found for each of the five  $\sigma_t$  values presented. The more precisely the time-of-flight is measured in the calorimeter, the better this point is determined. Indeed, the worse this resolution is, the more linear the distribution tends to be, and therefore the more difficult it is to discriminate delayed events from those emitted simultaneously such as those of  $0\nu\beta\beta$ . Especially, for an ideal calorimeter where the timing measurement would be perfect, we could reach 80% of  $^{208}\text{Tl}$  rejection, while keeping 90% of signal events.



As discussed, the variations of  $P_{int}$  and  $P_{exp}$  are bound to the value of  $\sigma_t$ , thus the levels applied on  $P_{int}$  and  $P_{exp}$  must be adapted to match these variations. Eight  $P_{int}/P_{exp}$  biplots are given in Fig. 4.11, for  $\sigma_t = 0, 100, 300$  and  $400$  ps both for  $0\nu\beta\beta$  and  $^{208}\text{Tl}$   $2e$  selected topologies (the  $\sigma_t = 200$  ps case is already given in Fig. 4.8). Depending on  $\sigma_t$ , the area to be rejected moves towards higher values of  $P_{int}$ . Taking this into consideration, optimised values for  $P_{int}$  have been set up, summarised in Tab. 4.3. To find an optimal value of  $P_{exp}$  to be applied, several cut-

$\sigma_t$ (ps)	0	100	200	300	400
$P_{int}$ cut-off	[0.05 - 0.3]	[0.25 - 0.6]	[0.4 - 0.7]	[0.5 - 0.8]	[0.55 - 0.85]

Table 4.3: Range of  $P_{int}$  for which events are rejected. An additional cut-off with  $P_{int} < 0.01$  and  $P_{exp} < 0.01$  is also applied.

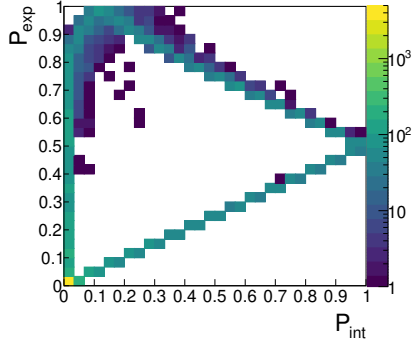
offs are set up from  $P_{exp} > 0$  to  $0.95$ , and associated with the  $P_{int}$  cut-offs presented in the previous table, in order to reject the required area. Following the work done for the  $\Delta t^{corr}$  cut-off, results are presented in Fig. 4.12 on an efficiency selection diagram. The calorimeter timing measurement has a great influence, especially on  $^{208}\text{Tl}$  events rejection. Evolution of selection efficiencies for  $\sigma_t < 200$  ps are very similar, reaching a plateau for  $\sim P_{exp} > 0.25$  allowing to reject 20% of  $^{208}\text{Tl}$  while keeping 85% of  $0\nu\beta\beta$ . Below  $\sigma = 100$  ps the background rejection is improved despite a loss in signal selection efficiency, up to reaching  $\sim 45\%$  of  $^{208}\text{Tl}$  rejection and  $\sim 80\%$  signal selection for an ideal calorimeter. The plateau is reached at  $P_{exp} > 0.2$  for  $\sigma_t = 100$  ps and  $P_{exp} > 0.15$  for  $\sigma_t = 0$  ps.

A better Thallium rejection can be obtained with the simple selection on time-of-flights, but the probability one has the main advantage to be more accurate as it takes into account the calorimeter time measurement uncertainties. Moreover, even if variations of selection/rejection of this diagram are not as pronounced as for the  $\Delta t^{corr}$  cut-off, a strong assumption can be made: the more we are precise on time-of-flight measurements, the more we are able to reject  $^{208}\text{Tl}$  events while keeping a satisfying part of signal. During the calorimeter R&D, a great effort has been made to improve the optical modules energy resolution compared to NEMO-3, notably because it allows to have a better background rejection, and thus to decrease its contribution to the  $0\nu\beta\beta$  search. Finally, in view of these results, a good timing precision in calorimeter blocks is also important when it concerns background rejection, and especially the identification of  $\beta$ -IC delayed  $^{208}\text{Tl}$  decays. Nevertheless, to give a final conclusion on the usefulness of the  $\Delta t^{corr}$  and probability cut-offs, one have to study its impact on the final sensitivity of the detector, which is dealt with in the next section.

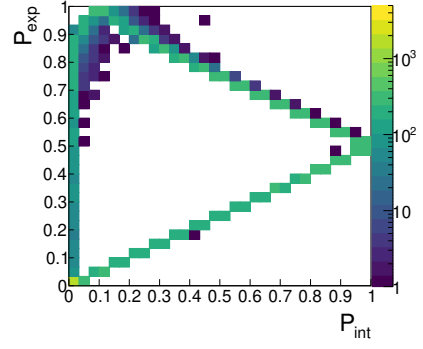
## 4.6 Impact of $^{208}\text{Tl}$ rejection on the experiment's sensitivity

In the previous sub-section were presented results for  $\Delta t^{corr}$  and optimised probability cut-offs, and the influence of the calorimeter time resolution on these rejection techniques was reviewed. Nevertheless, to properly quantify the

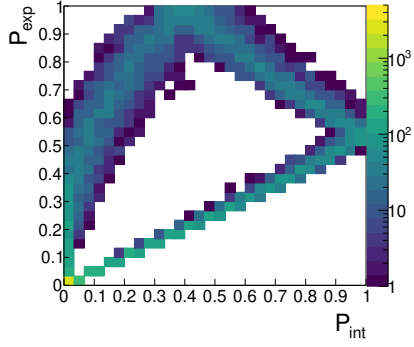
#### 4. IMPROVEMENT OF THE INTERNAL THALLIUM-208 BACKGROUND REJECTION



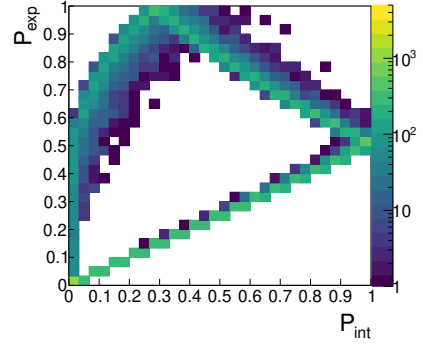
(a)  $^{208}\text{Tl}$  simulations,  $\sigma_t = 0$  ps.



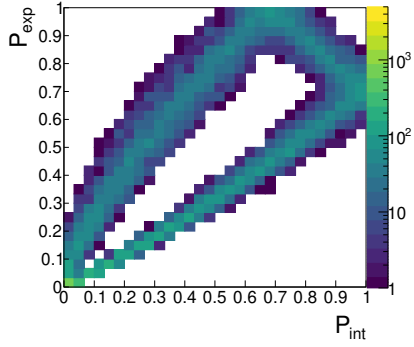
(b)  $0\nu\beta\beta$  simulations,  $\sigma_t = 0$  ps.



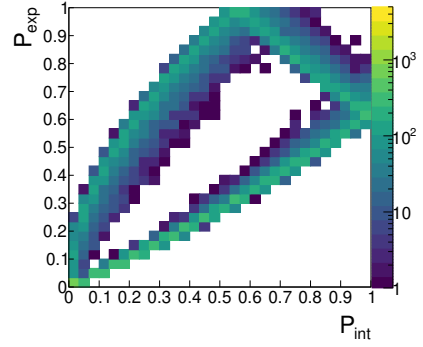
(c)  $^{208}\text{Tl}$  simulations,  $\sigma_t = 100$  ps.



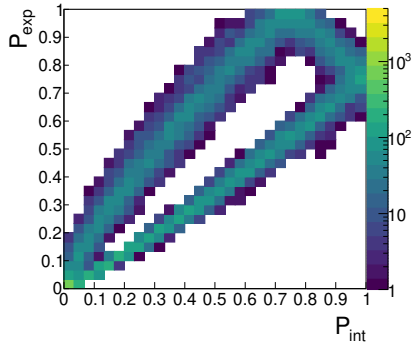
(d)  $0\nu\beta\beta$  simulations,  $\sigma_t = 100$  ps.



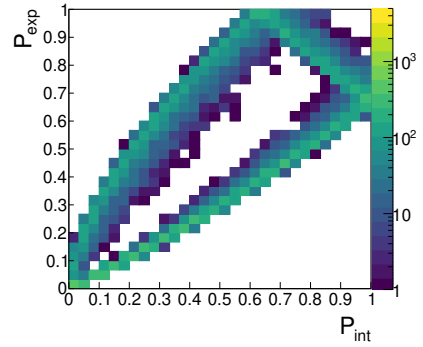
(e)  $^{208}\text{Tl}$  simulations,  $\sigma_t = 300$  ps.



(f)  $0\nu\beta\beta$  simulations,  $\sigma_t = 300$  ps.



(g)  $^{208}\text{Tl}$  simulations,  $\sigma_t = 400$  ps.



(h)  $0\nu\beta\beta$  simulations,  $\sigma_t = 400$  ps.

Figure 4.11:  $P_{int}/P_{exp}$  biplots for different  $\sigma_t$  values for  $^{208}\text{Tl}$  and  $0\nu\beta\beta$  simulations.

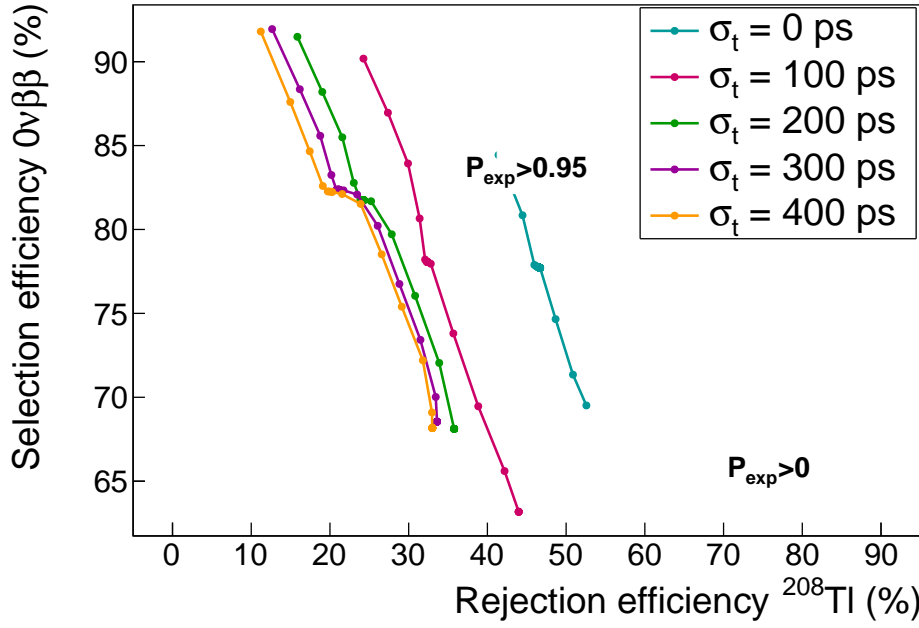


Figure 4.12:  $0\nu\beta\beta$  selection efficiency as a function of  $^{208}\text{Tl}$  rejection. Each point corresponds to a minimal  $P_{exp}$  value applied on the selected  $2e$  topologies.  $P_{int}$  selections are also applied, their value depending on the  $\sigma_t$  value (Tab. 4.3).  $\sigma_l = 27.8$  ps.

effectiveness of these cut-off, one have to study their impact on the final detector sensitivity (500 kg.y exposure). To do so, the procedure described in Chapter 3 is applied to the  $2e$  topologies selected (after the application of  $\Delta t^{corr}$  or probability cut-offs), for signal and backgrounds considered ( $2\nu\beta\beta$ ,  $^{214}\text{Bi}$ ,  $^{208}\text{Tl}$  and  $^{222}\text{Rn}$ ).

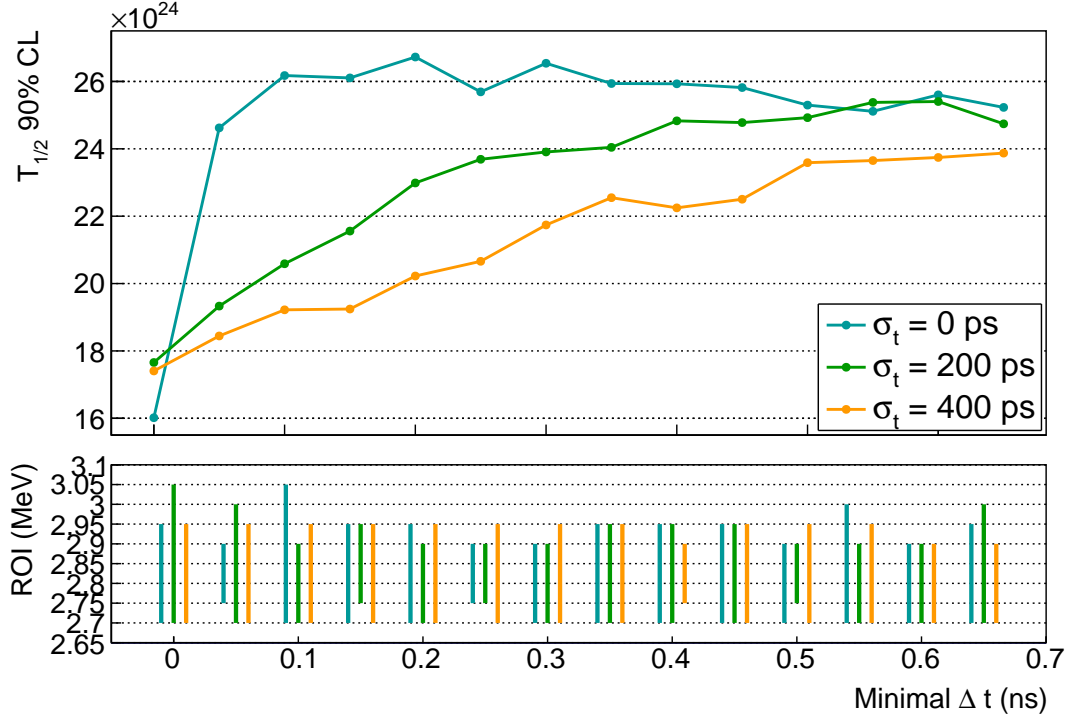
#### 4.6.1 Sensitivity results

The variations of the sensitivity are presented in Fig. 4.13 for three values of  $\sigma_t$  at 1 MeV, as a function of the cut-off levels applied. For these two figures, the more the  $x$ -values increase, the more the applied cut is released. In both cases sensitivity results converge towards  $\sim 2.4 \times 10^{25}$  years, for very loose values of the selection.

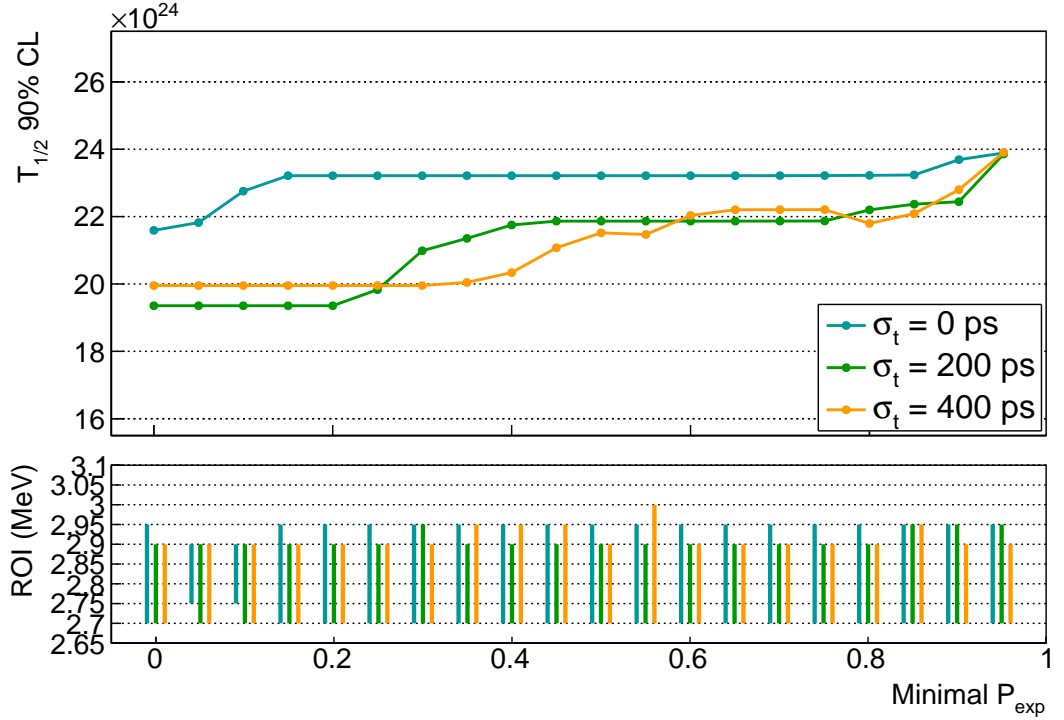
Regarding the influence of  $\Delta t^{corr}$  selection, a sensitivity improvement can eventually be obtained by applying this selection, depending on the value of  $\sigma_t$  considered for the calorimeter (Fig. 4.13a).

- $\sigma_t = 0$  ps at 1 MeV: an improvement of 12% on the sensitivity is observed for events rejected if  $\Delta t^{corr} > 200$  ps. This is consistent with the  $^{208}\text{Pb}$  metastable level of 294 ps to which we are very sensitive with such ideal value of the calorimeter resolution.
- $\sigma_t = 200$  ps at 1 MeV: a slighter improvement of 6% is reached for  $\Delta t^{corr} > 550$  ps. As the calorimeter time resolution is reduced, compared with the first ideal case, a smaller improvement can be obtained, for a loose value of the applied cut.

#### 4. IMPROVEMENT OF THE INTERNAL THALLIUM-208 BACKGROUND REJECTION



(a)  $\Delta t^{corr}$  cut-off.



(b) Probability cut-off.

Figure 4.13: (Top pad)  $T_{1/2}^{0\nu}$  at 90% CL and (bottom pad) optimised ROI, as a function of the minimal value of  $\Delta t$  applied on the selected  $2e$  topologies. Results are given for  $\sigma_t = 0, 200$  and  $400$  ps at  $1$  MeV, and  $\sigma_l = 27.8$  ps.

- $\sigma_t = 400$  ps at 1 MeV: the resolution is too degraded for an improvement to be obtained with such a time-of-flight cut-off.

Concerning the influence of probability selection, values of  $T_{1/2}^{0\nu}$  also converge towards a unique value, attained for  $P_{exp} > 1$ , meaning all the events are selected for such a level. In other words, the more restrictive this cut is, the more the sensitivity is reduced. The least unfavourable case is obtained for the ideal calorimeter resolution case, with stagnation of the values on a plateau, for most of the applied cut-off levels. Even if it is less wide, a plateau is also reached for  $\sigma_t = 200$  ps.

### 4.6.2 Expected number of background

The influence of the  $\Delta t^{corr}$  selection on the number of expected background events in the optimised ROI is presented in Tab. 4.4. Three values of  $\sigma_t$  are

$\sigma_t$ (ps)	0	200	400
ROI (MeV)	[2.7;2.95]	[2.7;2.9]	[2.7;2.95]
Minimal $\Delta t^{corr}$ (ps)	200	550	650
$T_{1/2}^{0\nu}$ (90% CL) ( $\times 10^{25}$ y)	2.7	2.5	2.4
$m_{\beta\beta}$ (90% CL) (eV)	[0.11 – 0.22]	[0.11 – 0.22]	[0.12 – 0.23]
$\epsilon_{0\nu}$	14.6%	14.2%	12.9%
$2\nu\beta\beta$	10.8	10.8	9.58
$^{208}\text{Tl}$	9.52	13.3	13.4
$^{214}\text{Bi}$	42.9	42.0	39.2
$^{222}\text{Rn}$	1.12	1.12	1.04
Total	64.4	67.2	63.2

Table 4.4: Expected number of background events in the optimised ROI, for the exposure of the SuperNEMO final detector (500 kg.y). Three values of  $\sigma_t$  are considered for which the best  $\Delta t^{corr}$  is applied.

considered, and for each of them the best level for this cut, determined in the previous sub-section, is applied. The best rejection of Thallium is reached for the ideal calorimeter time resolution, as the two electrons time-of-flights are measured precisely. For  $\sigma_t = 200$  ps, a smaller amount of Thallium background is rejected, but the  $0\nu\beta\beta$  selection efficiency remains stable. This selection efficiency is affected when the time resolution is degraded to  $\sigma_t$ , thus when the delayed events are badly discriminated compared with the simultaneous ones. As expected, other background events ( $2\nu\beta\beta$ ,  $^{214}\text{Bi}$  and  $^{222}\text{Rn}$ ) are not significantly affected by this selection.

As discussed, the probability cut-offs applied on  $2e$  topologies only degrade the final sensitivity to the  $0\nu\beta\beta$  process. To quantify its impact on the background rejection, we present in Tab. 4.5 the expected number of background in the optimised ROI, for two different levels for the  $P_{exp}$  selection, one at 0.5 and the other one very loose. Even if it affect the  $0\nu\beta\beta$  selection efficiency, this selection allows to reject 5 events of  $^{208}\text{Tl}$  inside the ROI for the SuperNEMO final detector.

#### 4. IMPROVEMENT OF THE INTERNAL THALLIUM-208 BACKGROUND REJECTION

ROI (MeV)	[2.7;2.9]	[2.7;2.9]
Minimal $P_{exp}$	0.5	0.95
$T_{1/2}^{0\nu}$ (90% CL) ( $\times 10^{25}$ y)	2.2	2.4
$m_{\beta\beta}$ (90% CL) (eV)	[0.12 – 0.24]	[0.12 – 0.23]
$\epsilon_{0\nu}$	12.1%	13.9%
$2\nu\beta\beta$	9.83	10.8
$^{208}\text{Tl}$	16.3	21.0
$^{214}\text{Bi}$	38.4	42.0
$^{222}\text{Rn}$	0.596	0.596
Total	65.1	74.4

Table 4.5: Expected number of background events in the optimised ROI, for the exposure of the SuperNEMO final detector (500 kg.y). The time resolution is taken as  $\sigma_t = 200$  ps. Two levels of  $P_{exp}$  cut are compared, 0.5 and 0.95.

These two selections were implemented in order to reject  $^{208}\text{Tl}$  events and they have fulfilled this role. The  $\Delta t^{corr}$  selection allowed to improve the sensitivity by 12% for a perfect calorimeter time resolution. Finally, the final detector sensitivity is greatly affected by this timing measurement precision.

## 4.7 Conclusion

During this chapter we have defined or specified analysis tools adapted to the rejection of background. In particular, a so-called exponential probability law has been defined to describe the internal events of delayed Thallium. Although the cut-off based on the electron time-of-flight is very satisfactory for rejecting this last background, the associated cut-off in internal and exponential probability makes it possible to be more precise since it takes into account the errors made on the time-of-flight measurements in the calorimeter. These rejection could be tested on site using a  $^{232}\text{U}$  calibration source, a parent of  $^{208}\text{Tl}$  nucleus, inside the calorimeter to check the  $^{208}\text{Tl}$  rejection using time-of-flight.

We have determined the influence the time resolution has on the various defined cut-off efficiencies. The worse this resolution is, the more difficult it is to discriminate thallium events from signal events. Improving the time resolution of the calorimeter was not a direct purpose of the R&D programme, however it has benefited from the high light output achieved to meet the energy resolution goals. The time resolution of the optical modules has been monitored at every stage of the R&D programme but remains to be precisely determined. This is precisely the purpose of the next chapter, which describes how we determined the time resolution of the optical modules of the demonstrator calorimeter with a  $^{60}\text{Co}$  source.



---

## Bibliography

- [1] M. Agostini et al. Probing majorana neutrinos with double- $\beta$  decay. *Science* 365, 1445, 2019.
- [2] S.I. Alvis et al. Search for neutrinoless double-beta decay in  $^{76}\text{Ge}$  with 26 kg-yr of exposure from the majorana demonstrator. *Phys. Rev. C*, 100, 2019.
- [3] O. Azzolini et al. First result on the neutrinoless double- $\beta$  decay of  $^{82}\text{Se}$  with cupid-0. *Phys. Rev. Lett.*, 120:232502, Jun 2018.
- [4] C. Alduino et al. First results from cuore: A search for lepton number violation via  $0\nu\beta\beta$  decay of  $^{130}\text{Te}$ . *Phys. Rev. Lett.*, 120:132501, Mar 2018.
- [5] J. B. Albert et al. Search for neutrinoless double-beta decay with the upgraded exo-200 detector. *Phys. Rev. Lett.*, 120:072701, Feb 2018.
- [6] A. Gando et al. Search for majorana neutrinos near the inverted mass hierarchy region with kamland-zen. *Phys. Rev. Lett.*, 117:082503, Aug 2016.
- [7] Chopra A. C0 commissioning results. Internal presentation, 2015.
- [8] Cerna C. Tracker review conclusions. Internal presentation, 2014.
- [9] S. Clavez. *Development of reconstruction tools and sensitivity of the SuperNEMO demonstrator*. PhD thesis, Université Paris Sud, 2017.
- [10] Garrido X. Bongrand M. Hamamatsu 8" pmt test in magnetic shield. Internal presentation, 2014.
- [11] Loaiza P. Source foils measurement with bipo. Internal presentation, 2017.
- [12] Perrot F. Radiopurity measurements for 8" pmcs and preliminary budget for the sn demonstrator. Internal presentation, 2017.
- [13] et al Arnold R. Technical design and performance of the nemo3 detector. *Nucl. Instrum. Meth. A*, pages 79–122, 2005.
- [14] Xin Ran Liu. Radon mitigation strategy and results for the supernemo experiment. IoP APP / HEPP Conference, 2018.



- [15] A. Huber. *Recherche de la nature du neutrino avec le détecteur SuperNEMO : Simulations optiques pour l'optimisation du calorimètre et performances attendues pour le  $^{82}\text{Se}$* . PhD thesis, Université Bordeaux, 2017.
- [16] R. Arnold et al. Probing new physics models of neutrinoless double beta decay with supernemo. *Eur. Phys. J. C*, 2010.
- [17] Tretyak V.I. Ponkratenko O.A. and Zdesenko Yu.G. The event generator decay4 for simulation of doublebeta processes and decay of radioactive nuclei. *Phys. At. Nucl.*, 63:1282–1287, Jul 2000.
- [18] R. Arnold et al. Results of the search for neutrinoless double- $\beta$  decay in  $^{100}\text{mo}$  with the nemo-3 experiment. *Phys. Rev. D*, 2015.
- [19] Gomez-Cadenas et al. Physics case of supernemo with  $^{82}\text{se}$  source. Internal presentation, 2008.
- [20] R. Arnold et al. Final results on  $^{82}\text{se}$  double beta decay to the ground state of  $^{82}\text{kr}$  from the nemo-3 experiment. *Eur. Phys. J. C*, 2018.
- [21] Cousins D. Feldman G. A unified approach to the classical statistical analysis of small signals. *Phys.Rev.*, pages 3873–3889, 1999.
- [22] J. Kotila and F. Iachello. Phase-space factors for double- $\beta$  decay. *Phys. Rev. C*, 85:034316, Mar 2012.
- [23] Dong-Liang Fang, Amand Faessler, Vadim Rodin, and Fedor Šimkovic. Neutrinoless double- $\beta$  decay of deformed nuclei within quasiparticle random-phase approximation with a realistic interaction. *Phys. Rev. C*, 83:034320, Mar 2011.
- [24] A. Chapon. *Mesure des processus de double désintégration bêta du Mo vers l'état excité  $0_1^+$  du Ru dans l'expérience Nemo3, Programme de R&D SuperNEMO : mise au point d'un détecteur BiPo pour la mesure de très faibles contaminations de feuilles sources*. PhD thesis, Université Caen Basse-Normandie, 2011.
- [25] Snow S. A magnetic field map for the tracker. Internal presentation, 2015.
- [26] A. Pin. *Recherche de la nature du neutrino via la décroissance double bêta sans émission de neutrinos. Caractérisation et optimisation du calorimètre SuperNEMO et impact sur la recherche de la décroissance du  $^{82}\text{Se}$  Développement du premier prototype LiquidO*. PhD thesis, Université Bordeaux-Gradignan, 2020.
- [27] A. H. Wapstra G. Audi. The 1995 update to the atomic mass evaluation. *Nucl. Phys. A*, 595:409–480, feb 1995.
- [28] R. Arnold et al. Measurement of the  $2\nu\beta\beta$  decay half-life of  $^{150}\text{nd}$  and a search for  $0\nu\beta\beta$  decay processes with the full exposure from the nemo-3 detector. *Phys. Rev. D*, 94, oct 2016.

- [29] Estar database (nist). <http://physics.nist.gov/PhysRefData/Star/Text/ESTAR.html>.
- [30] Xcom database (nist). <http://physics.nist.gov/PhysRefData/Xcom/html/xcom1.html>.
- [31] Nucleid database.
- [32] My github page. <https://github.com/girardcarillo>.